An IXPE-Led X-ray Spectro-Polarimetric Campaign on the Soft State of Cygnus X-1: X-ray Polarimetric Evidence for Strong Gravitational Lensing

James F Steiner, Edward Nathan, Kun Hu, Henric Krawczynski, Michal Dovciak, Alexandra Veledina, Fabio Muleri, Jiri Svoboda, Kevin Alabarta, Maxime Parra, et al.

The Astrophysical Journal Letters, 969:L30 (15pp), 2024 July 10 https://doi.org/10.3847/2041-8213/ad58e4

An IXPE-led X-Ray Spectropolarimetric Campaign on the Soft State of Cygnus X-1: X-Ray Polarimetric Evidence for Strong Gravitational Lensing

James F. Steiner[1], Edward Nathan[2], Kun Hu[3], Henric Krawczynski[3], Michal Dovčiak[4], Alexandra Veledina[5,6], Fabio Muleri[7], Jiri Svoboda[4], Kevin Alabarta[8], Maxime Parra[9,10], Yash Bhargava[11], Giorgio Matt[10], Juri Poutanen[5], Pierre-Olivier Petrucci[9], Allyn F. Tennant[12], M. Cristina Baglio[13], Luca Baldini[14,15], Samuel Barnier[9], Sudip Bhattacharyya[11], Stefano Bianchi[10], Maimouna Brigitte[4], Mauricio Cabezas[16], Floriane Cangemi[17], Fiamma Capitanio[7], Jacob Casey[18], Nicole Rodriguez Cavero[3], Simone Castellano[14], Elisabetta Cavazzuti[19], Sohee Chun[3], Eugene Churazov[20], Enrico Costa[7], Niccolò Di Lalla[21], Alessandro Di Marco[7], Elise Egron[22], Melissa Ewing[23], Sergio Fabiani[7], Javier A. García[24], David A. Green[25], Victoria Grinberg[26], Petr Hadrava[4], Adam Ingram[23], Philip Kaaret[12], Fabian Kislat[18], Takao Kitaguchi[27], Vadim Kravtsov[5], Brankica Kubátová[16], Fabio La Monaca[7,28,29], Luca Latronico[30], Vladislav Loktev[5], Christian Malacaria[31], Frédéric Marin[32], Andrea Marinucci[19], Olga Maryeva[16], Guglielmo Mastroserio[22], Tsunefumi Mizuno[33], Michela Negro[34], Nicola Omodei[21], Jakub Podgorný[4,32,35], John Rankin[7], Ajay Ratheesh[7], Lauren Rhodes[36], David M. Russell[8], Miroslav Šlechta[16], Paolo Soffitta[7], Sean Spooner[18], Valery Suleimanov[37], Francesco Tombesi[28,38,39], Sergei A. Trushkin[40,41], Martin C. Weisskopf[12], Silvia Zane[42], Andrzej A. Zdziarski[43], Sixuan Zhang[33], Wenda Zhang[44], Menglei Zhou[37], Iván Agudo[45], Lucio A. Antonelli[46,47], Matteo Bachetti[48], Wayne H. Baumgartner[12], Ronaldo Bellazzini[14], Stephen D. Bongiorno[12], Raffaella Bonino[30,49], Alessandro Brez[14], Niccolò Bucciantini[50,51,52], Chien-Ting Chen[53], Stefano Ciprini[38,47], Alessandra De Rosa[7], Ettore Del Monte[7], Laura Di Gesu[19], Immacolata Donnarumma[19], Victor Doroshenko[37], Steven R. Ehlert[12], Teruaki Enoto[27], Yuri Evangelista[7], Riccardo Ferrazzoli[7], Shuichi Gunji[54], Kiyoshi Hayashida[55,69], Jeremy Heyl[56], Wataru Iwakiri[57], Svetlana G. Jorstad[58,59], Vladimir Karas[4], Jeffery J. Kolodziejczak[12,28,29], Ioannis Liodakis[12], Simone Maldera[30], Alberto Manfreda[60], Alan P. Marscher[58], Herman L. Marshall[61], Francesco Massaro[30,49], Ikuyuki Mitsuishi[62], Chi-Yung Ng[63], Stephen L. O'Dell[12], Chiara Oppedisano[30], Alessandro Papitto[46], George G. Pavlov[64], Abel L. Peirson[21], Matteo Perri[46,47], Melissa Pesce-Rollins[14], Maura Pilia[48], Andrea Possenti[48], Simonetta Puccetti[47], Brian D. Ramsey[12], Oliver J. Roberts[53], Roger W. Romani[21], Carmelo Sgrò[14], Patrick Slane[1], Gloria Spandre[14], Douglas A. Swartz[53], Toru Tamagawa[27], Fabrizio Tavecchio[65], Roberto Taverna[66], Yuzuru Tawara[62], Nicholas E. Thomas[12], Alessio Trois[48], Sergey S. Tsygankov[5], Roberto Turolla[42,66], Jacco Vink[67], Kinwah Wu[42], and Fei Xie[7,68]

[1] Center for Astrophysics | Harvard & Smithsonian, 60 Garden Street, Cambridge, MA 02138, USA; jsteiner@cfa.harvard.edu
[2] California Institute of Technology, Pasadena, CA 91125, USA
[3] Physics Department, McDonnell Center for the Space Sciences, and Center for Quantum Leaps, Washington University in St. Louis, St. Louis, MO 63130, USA
[4] Astronomical Institute of the Czech Academy of Sciences, Boční II 1401/1, 14100 Praha 4, Czech Republic
[5] Department of Physics and Astronomy, 20014 University of Turku, Finland
[6] Nordita, KTH Royal Institute of Technology and Stockholm University, Hannes Alfvéns väg 12, SE-10691 Stockholm, Sweden
[7] INAF Istituto di Astrofisica e Planetologia Spaziali, Via del Fosso del Cavaliere 100, 00133 Roma, Italy
[8] Center for Astrophysics and Space Science (CASS), New York University Abu Dhabi, PO Box 129188, Abu Dhabi, UAE
[9] Université Grenoble Alpes, CNRS, IPAG, 38000 Grenoble, France
[10] Dipartimento di Matematica e Fisica, Universitá degli Studi Roma Tre, Via della Vasca Navale 84, 00146 Roma, Italy
[11] Department of Astronomy and Astrophysics, Tata Institute of Fundamental Research, 1 Homi Bhabha Road, Colaba, 400005 Mumbai, India
[12] NASA Marshall Space Flight Center, Huntsville, AL 35812, USA
[13] INAF-Osservatorio Astronomico di Brera, Via Bianchi 46, I-23807 Merate (LC), Italy
[14] Istituto Nazionale di Fisica Nucleare, Sezione di Pisa, Largo B. Pontecorvo 3, 56127 Pisa, Italy
[15] Dipartimento di Fisica, Università di Pisa, Largo B. Pontecorvo 3, 56127 Pisa, Italy
[16] Astronomical Institute of the Czech Academy of Sciences, Ondřejov Observatory, Fričova 298, 251 65 Ondřejov, Czech Republic
[17] Université Paris-Cité, APC, 10 Rue Alice Domon et Léonie Duquet, 75013 Paris, France
[18] Department of Physics and Astronomy and Space Science Center, University of New Hampshire, Durham, NH 03824, USA
[19] Agenzia Spaziale Italiana, Via del Politecnico snc, 00133 Roma, Italy
[20] Max Planck Institute for Astrophysics, Karl-Schwarzschild-Str. 1, D-85741 Garching, Germany
[21] Department of Physics and Kavli Institute for Particle Astrophysics and Cosmology, Stanford University, Stanford, CA 94305, USA
[22] INAF-Osservatorio Astronomico di Cagliari, Via della Scienza 5, I-09047 Selargius (CA), Italy
[23] School of Mathematics, Statistics, and Physics, Newcastle University, Newcastle upon Tyne NE1 7RU, UK
[24] X-Ray Astrophysics Laboratory, NASA Goddard Space Flight Center, Greenbelt, MD 20771, USA
[25] Cavendish Laboratory, University of Cambridge, 19 J.J. Thomson Avenue, Cambridge, CB3 0HE, UK
[26] European Space Agency (ESA), European Space Research and Technology Centre (ESTEC), Keplerlaan 1, 2201 AZ Noordwijk, The Netherlands
[27] RIKEN Cluster for Pioneering Research, 2-1 Hirosawa, Wako, Saitama 351-0198, Japan
[28] Dipartimento di Fisica, Università degli Studi di Roma "Tor Vergata", Via della Ricerca Scientifica 1, 00133 Roma, Italy
[29] Dipartimento di Fisica, Università degli Studi di Roma "La Sapienza", Piazzale Aldo Moro 5, 00185 Roma, Italy
[30] Istituto Nazionale di Fisica Nucleare, Sezione di Torino, Via Pietro Giuria 1, 10125 Torino, Italy
[31] International Space Science Institute (ISSI), Hallerstrasse 6, 3012, Bern, Switzerland
[32] Université de Strasbourg, CNRS, Observatoire Astronomique de Strasbourg, UMR 7550, 67000 Strasbourg, France
[33] Hiroshima Astrophysical Science Center, Hiroshima University, 1-3-1 Kagamiyama, Higashi-Hiroshima, Hiroshima 739-8526, Japan
[34] Department of Physics and Astronomy, Louisiana State University, Baton Rouge, LA 70803, USA
[35] Astronomical Institute, Charles University, V Holešovičkách 2, CZ-18000, Prague, Czech Republic

[36] Astrophysics, The University of Oxford, Keble Road, Oxford, OX1 3RH, UK
[37] Institut für Astronomie und Astrophysik, Universität Tübingen, Sand 1, 72076 Tübingen, Germany
[38] Istituto Nazionale di Fisica Nucleare, Sezione di Roma "Tor Vergata", Via della Ricerca Scientifica 1, 00133 Roma, Italy
[39] Department of Astronomy, University of Maryland, College Park, MD 20742, USA
[40] Special Astrophysical Observatory, Russian Academy of Sciences, 369167, Nizhnii Arkhyz, Russia
[41] Kazan (Volga Region) Federal University, 420008, Kazan, Russia
[42] Mullard Space Science Laboratory, University College London, Holmbury St Mary, Dorking, Surrey RH5 6NT, UK
[43] Nicolaus Copernicus Astronomical Center, Polish Academy of Sciences, Bartycka 18, PL-00-716 Warsaw, Poland
[44] National Astronomical Observatories, Chinese Academy of Sciences, Beijing 100101, People's Republic of China
[45] Instituto de Astrofísica de Andalucía—CSIC, Glorieta de la Astronomía s/n, 18008 Granada, Spain
[46] INAF Osservatorio Astronomico di Roma, Via Frascati 33, 00040 Monte Porzio Catone (RM), Italy
[47] Space Science Data Center, Agenzia Spaziale Italiana, Via del Politecnico snc, 00133 Roma, Italy
[48] INAF Osservatorio Astronomico di Cagliari, Via della Scienza 5, 09047 Selargius (CA), Italy
[49] Dipartimento di Fisica, Università degli Studi di Torino, Via Pietro Giuria 1, 10125 Torino, Italy
[50] INAF Osservatorio Astrofisico di Arcetri, Largo Enrico Fermi 5, 50125 Firenze, Italy
[51] Dipartimento di Fisica e Astronomia, Università degli Studi di Firenze, Via Sansone 1, 50019 Sesto Fiorentino (FI), Italy
[52] Istituto Nazionale di Fisica Nucleare, Sezione di Firenze, Via Sansone 1, 50019 Sesto Fiorentino (FI), Italy
[53] Science and Technology Institute, Universities Space Research Association, Huntsville, AL 35805, USA
[54] Yamagata University, 1-4-12 Kojirakawa-machi, Yamagata-shi 990-8560, Japan
[55] Osaka University, 1-1 Yamadaoka, Suita, Osaka 565-0871, Japan
[56] University of British Columbia, Vancouver, BC V6T 1Z4, Canada
[57] International Center for Hadron Astrophysics, Chiba University, Chiba 263-8522, Japan
[58] Institute for Astrophysical Research, Boston University, 725 Commonwealth Avenue, Boston, MA 02215, USA
[59] Department of Astrophysics, St. Petersburg State University, Universitetsky pr. 28, Petrodvoretz, 198504 St. Petersburg, Russia
[60] Istituto Nazionale di Fisica Nucleare, Sezione di Napoli, Strada Comunale Cinthia, 80126 Napoli, Italy
[61] MIT Kavli Institute for Astrophysics and Space Research, Massachusetts Institute of Technology, 77 Massachusetts Avenue, Cambridge, MA 02139, USA
[62] Graduate School of Science, Division of Particle and Astrophysical Science, Nagoya University, Furo-cho, Chikusa-ku, Nagoya, Aichi 464-8602, Japan
[63] Department of Physics, The University of Hong Kong, Pokfulam, Hong Kong
[64] Department of Astronomy and Astrophysics, Pennsylvania State University, University Park, PA 16801, USA
[65] INAF Osservatorio Astronomico di Brera, via E. Bianchi 46, 23807 Merate (LC), Italy
[66] Dipartimento di Fisica e Astronomia, Università degli Studi di Padova, Via Marzolo 8, 35131 Padova, Italy
[67] Anton Pannekoek Institute for Astronomy & GRAPPA, University of Amsterdam, Science Park 904, 1098 XH Amsterdam, The Netherlands
[68] Guangxi Key Laboratory for Relativistic Astrophysics, School of Physical Science and Technology, Guangxi University, Nanning 530004, People's Republic of China

Received 2024 February 16; revised 2024 June 7; accepted 2024 June 16; published 2024 July 5

Abstract

We present the first X-ray spectropolarimetric results for Cygnus X-1 in its soft state from a campaign of five IXPE observations conducted during 2023 May–June. Companion multiwavelength data during the campaign are likewise shown. The 2–8 keV X-rays exhibit a net polarization degree PD = 1.99% ± 0.13% (68% confidence). The polarization signal is found to increase with energy across the Imaging X-ray Polarimetry Explorer's (IXPE) 2–8 keV bandpass. The polarized X-rays exhibit an energy-independent polarization angle of PA = $-25\overset{\circ}{.}7 \pm 1\overset{\circ}{.}8$ east of north (68% confidence). This is consistent with being aligned to Cyg X-1's au-scale compact radio jet and its parsec-scale radio lobes. In comparison to earlier hard-state observations, the soft state exhibits a factor of 2 lower polarization degree but a similar trend with energy and a similar (also energy-independent) position angle. When scaling by the natural unit of the disk temperature, we find the appearance of a consistent trend line in the polarization degree between the soft and hard states. Our favored polarimetric model indicates that Cyg X-1's spin is likely high ($a_* \gtrsim 0.96$). The substantial X-ray polarization in Cyg X-1's soft state is most readily explained as resulting from a large portion of X-rays emitted from the disk returning and reflecting off the disk surface, generating a high polarization degree and a polarization direction parallel to the black hole spin axis and radio jet. In IXPE's bandpass, the polarization signal is dominated by the returning reflection emission. This constitutes polarimetric evidence for strong gravitational lensing of X-rays close to the black hole.

Unified Astronomy Thesaurus concepts: Accretion (14); Polarimetry (1278); X-ray astronomy (1810); Stellar mass black holes (1611)

1. Introduction

In a recent pioneering study of the hard state of Cygnus X-1 (hereafter Cyg X-1), the Imaging X-ray Polarimetry Explorer (IXPE; Weisskopf et al. 2022) produced the first unambiguous soft X-ray polarimetric detection of a black hole (BH) and, moreover, measured a significant increase in the degree of polarization across IXPE's 2–8 keV bandpass (Krawczynski et al. 2022). An accompanying set of NICER and NuSTAR observations spanning the campaign proved key to deciphering the IXPE results by identifying the source of polarized emission (the corona, or possibly a hot flow) and thereby enabling a spectropolarimetric constraint on the geometry of the inner accretion flow (i.e., the inner disk and its enshrouding hot-electron corona). These first-of-their-kind measurements included several surprising results, foremost the unexpectedly strong polarization at 4%. These results were able to unambiguously rule out (for the hard state) a popular

[69] Deceased.

"lamppost" model for the corona's geometry in Cyg X-1. Here, we report a cousin campaign again led by IXPE to explore the X-ray polarimetric signature of Cyg X-1's soft state.

Cyg X-1 is the brightest persistent BH source in the Galaxy at ∼0.2–2 Crab (2–20 keV) and the first X-ray binary widely accepted to harbor an accreting BH (Bolton 1972; Webster & Murdin 1972). Its X-ray emission is fueled by the accretion of powerful winds from its O supergiant companion (Orosz et al. 2011). A recent parallax study by Miller-Jones et al. (2021) yielded a precise distance of $D = 2.2 \pm 0.2$ kpc and a refined BH mass of $M = 21.2 \pm 2.2\,M_{\odot}$ with a companion mass of $41 \pm 7\,M_{\odot}$. This marks Cyg X-1 as the most massive BH among currently known X-ray binaries.

From Cyg X-1's proper motion in the Galaxy, Miller-Jones et al. (2021) strongly constrain Cyg X-1's natal kick, $v < 10-20\,\mathrm{km\,s^{-1}}$ (see also Mirabel & Rodrigues 2003). This indicates that any misalignment of the spin and binary orbital angular momentum of the nascent Cyg X-1 should be slight, at most $\phi \lesssim 10^{\circ}$ when formed. This result is significant in light of a precise orbital inclination measurement via ellipsoidal light-curve modeling (Orosz et al. 2011), $i_{\rm orb} \approx 27^{\circ} \pm 1^{\circ}$.

Across decades of X-ray monitoring, Cyg X-1 has been found to range by an order of magnitude in its X-ray flux, typically accreting at a few percent of its Eddington limit. Such a range is, however, remarkably constant in comparison to the >6 orders of magnitude traversed in the outburst of a typical BH transient. At the same time, unlike the other wind-fed BHs, Cyg X-1's low mass accretion rate causes it to range along the lower track of BH hardness–intensity, producing intermittent state transitions.

In fact, Cyg X-1's state changes were prototypical for establishing a hard/soft-state dichotomy (Tananbaum et al. 1972). While this behavior served as an archetype for establishing the hard and soft spectral states ubiquitous among X-ray binaries (Oda 1977), its soft state never reaches the extremity of the long-lived "thermal-dominant" state common among BH X-ray transients, in which the coronal X-ray contribution is minimal. Instead, Cyg X-1's soft state is associated with the canonical "steep power law" (SPL) or sometimes "soft-intermediate" state (Fender et al. 2004; Remillard & McClintock 2006).

Broadly, hard states are dominated by emission Comptonized in a hot corona and exhibit radio jets, whereas soft states are dominated by thermal disk emission and present weak or no radio-jet activity (Fender et al. 2004). Cyg X-1 regularly presents a compact radio jet in its soft state (Zdziarski et al. 2020). Compared to hard states, the soft-state disk temperature is generally higher, while the coronal emission is both weaker and spectrally steeper. Wide-ranging evidence on spectral and timing grounds implies that state transitions are associated with significant changes in the geometry of the innermost accretion flow (e.g., Ichimaru 1977; De Marco et al. 2015; Méndez et al. 2022; Wang et al. 2022). At the same time, the nature of such structural changes as well as the location and shape of the corona are contentious, possibly involving the truncation of the inner accretion disk at radii much larger than the innermost stable circular orbit (ISCO; e.g., García et al. 2015; Basak & Zdziarski 2016) and with candidate coronal geometries ranging from sphere to slab to lamppost (e.g., Poutanen & Svensson 1996; Dove et al. 1997; Dauser et al. 2016).

Cyg X-1's hard and soft states commonly persist for weeks to years at a time. Despite the slow pace of interstate evolution, both its hard and soft states exhibit substantial intrastate secular variations in intensity and hardness over timescales from hours to days, and its power-density spectrum shows a pronounced broad feature near ∼1 Hz (e.g., Grinberg et al. 2014). In the soft state, Cyg X-1's disk is expected to reach the ISCO. The disk produces a quasi-blackbody spectrum that dominates $\lesssim$3 keV, with higher energies indicating the presence of a corona with hybrid thermal/nonthermal electrons (Poutanen & Coppi 1998; Gierliński et al. 1999). The disk-dominated spectrum can be modeled via continuum fitting to determine the radius of the ISCO, which is linked to BH spin (Zhang et al. 1997; Gou et al. 2014). The ISCO radius is also traced by the relativistic broadening of "reflection" features. These were first discovered in Cyg X-1 (Barr et al. 1985) and arise from X-ray irradiation reprocessing in the accretion disk's surface (Fabian et al. 1989). Typically, this X-ray source is the corona, but it could in some instances be returning radiation from the disk illuminating itself (Cunningham 1976; Connors et al. 2020; Krawczynski & Beheshtipour 2022).

Numerous X-ray spectroscopic studies have explored the question of Cyg X-1's dimensionless spin parameter ($a_* \equiv \frac{cJ}{GM^2}$). Continuum-fitting studies focused on the thermal disk emission in soft states (Zhang et al. 1997; McClintock et al. 2006) consistently find a near-maximal value ($a_* \gtrsim 0.98$; Gou et al. 2011, 2014; Zhao et al. 2021). This conclusion has been supported by numerous reflection studies as well, including analyses of both hard and soft states (e.g., Fabian et al. 2012; Tomsick et al. 2014; Walton et al. 2016; Basak et al. 2017; Tomsick et al. 2018), but see Zdziarski et al. (2024). Some reflection fits suggest a possible ∼10° misalignment with the binary orbital plane, an interpretation also favored in our hard-state polarimetric study (Krawczynski et al. 2022).

Before IXPE's measurements, soft X-ray polarization in Cyg X-1 was tentatively detected (<99% confidence) by OSO-8 with a polarization degree (PD) of ∼2%–5% (Weisskopf et al. 1977; Long et al. 1980). At energies above $\gtrsim$200 keV, polarization for Cyg X-1's hard state has been studied using INTEGRAL with the INTEGRAL Soft Gamma-ray Imager (ISGRI) and SPectrometer on INTEGRAL instruments independently (Laurent et al. 2011; Jourdain et al. 2012; Rodriguez et al. 2015) and more recently by the AstroSat-CZTI in the 100–380 keV band (Chattopadhyay et al. 2024). At high energies, Cyg X-1 is found to be strongly polarized, and the PD is rising with energy. It is most prominent in the so-called "hard tail" above $\gtrsim$400 keV (i.e., excess emission above the Comptonization cutoff), where the PD exceeds 60%. The PoGO+ balloon-borne polarimeter constrained Cyg X-1's PD to <8.6% in the 19–181 keV range for its hard state (Chauvin et al. 2018). Polarization in the soft state at high energies could not be constrained with current INTEGRAL data due to low signal. Although a hard tail has been detected in the soft state (McConnell et al. 2002), constraints on its properties are model-dependent (Cangemi et al. 2021; see also Chattopadhyay et al. 2024).

This Letter is organized as follows. In Section 2, we detail our observational campaign and present the data. We show fits to these data and associated spectropolarimetric results in Section 3. We offer a discussion of these results in Section 4 and concluding remarks in Section 5.

2. Data

In 2023 April, Cyg X-1 transitioned from a long-lived hard state to the soft state, initiating a corresponding IXPE soft-state

Table 1
X-Ray Observations

Epoch	Date (UTC)	Orbital Phase	Mission	Instrument	Exposure Times ks	IXPE Count Rate s^{-1} (2–8 keV)	IXPE Hardness (4–8 keV/2–4 keV)
1	2023 May 2–3	0.81–0.90	IXPE	GPD	20.9	99	0.077
2	2023 May 9–10	0.97–0.09	IXPE	GPD	31.0	124	0.074
			Swift[a]	XRT	1.8		
3	2023 May 24–25	0.71–0.83	IXPE	GPD	24.8	166	0.042
			AstroSat	SXT/LAXPC	8.6/24.6		
			NICER	XTI	6.8		
			NuSTAR	FPMA+B	13.8		
4	2023 Jun 13–14	0.31–0.43	IXPE	GPD	28.7	146	0.057
			INTEGRAL	IBIS	24.7		
			NuSTAR	FPMA+B	9.5		
5	2023 Jun 20	0.39–0.54	IXPE	GPD	34.6	183	0.066
			INTEGRAL	IBIS	24.2		
			NICER	XTI	14.5		
			NuSTAR	FPMA+B	10.5		

Notes. IXPE exposure times have been corrected for detector dead time, and count IXPE rates are for IXPE's default "NEFF" weighting. Orbital phases are given from superior conjunction with the BH using the ephemeris of Brocksopp et al. (1999).
[a] Swift observed Cyg X-1 with XRT in windowed-timing mode; however, the data were heavily contaminated by photon pileup and did not yield reliable spectroscopy. While listed here for completeness, Swift XRT was not included in our analysis.

monitoring campaign. In order to prevent data-recorder overflow, the observation was broken into five epochs spanning 2023 May 2 through June 20. A preliminary look at the polarimetric results was posted in an Astronomer's Telegram (AT; Dovciak et al. 2023), motivating a rich multiwavelength campaign to supplement IXPE's later epochs, including complementary X-ray spectral coverage during epochs 3–5 with NuSTAR, NICER, INTEGRAL, AstroSat, and Swift, as summarized in Table 1. IXPE polarimetric results from epochs 1–3 were published by Jana & Chang (2024); their presentation of the polarimetric measurements is aligned with those of the AT and what we present here, although our conclusions differ from the ones of Jana & Chang (2024).

We focus our spectroscopic analysis on epochs 3–5, for which we have complementary broadband X-ray coverage. Low-energy data are particularly important to constrain Cyg X-1's thermal disk emission, which exhibits peak temperatures of $\lesssim$0.5 keV. The broadband spectral data in combination with IXPE's spectro-polarimetric information allow us to identify and constrain the different emission components. The net polarization of the soft/thermal state in the IXPE band depends on the polarization of the thermal disk emission, which is thought to exhibit a PD minimum and a large-amplitude (90°) swing of the polarization angle (PA) just above the thermal peak (e.g., Schnittman & Krolik 2009) and is also very sensitive to Compton scattering in the corona (Schnittman & Krolik 2010).

Broadband X-ray fits require coverage by missions other than IXPE and are crucial to disentangling the components of Cyg X-1's emission, particularly given that IXPE has coarse energy resolution ($\sim$20%) and is sensitive over a limited range of 2–8 keV. Compared to this, Cyg X-1's disk emission is cool and out of band, with temperatures $\lesssim$0.5 keV.[70] Accordingly, in Section 3, our spectroscopic analysis focuses on epochs 3–5.

The IXPE campaign was also supplemented with multi-wavelength monitoring carried out in the radio with RATAN-600 and the Arcminute Microkelvin Imager (AMI), with optical data from Las Cumbres Observatory (LCO), and with the Perek Telescope observing in narrowband Hα. Figure 1 presents radio and optical measurements of Cyg X-1 during the IXPE campaign. The radio jet, while faint, is significantly detected throughout. The Hα emission originates in the stellar wind and has been separated from emission by circumstellar matter and telluric lines using the disentangling method (see Hadrava 1997, 2009). These line strengths are an order of magnitude weaker than comparable data from the hard state.

In the right-hand panel, daily MAXI hardness and intensity measurements are shown, illustrating Cyg X-1's state bimodality, with the IXPE observations overlaid. Further details on each data set, including reduction procedures, are given in the Appendix.

3. Results

3.1. Polarimetric Data

IXPE observations were processed using the IXPEOBSSIM software (Baldini et al. 2022). For each observation, source events were extracted from an 80″ aperture centered on the source. Using IXPEOBSSIM, we obtain the background-subtracted Stokes parameters (see Section A.1) and calculate the PD and the PA per detector and energy interval of interest.

Figure 2 presents the PD and PA for Cyg X-1 across the five epochs, as determined from Stokes Q and U data. The left-hand panel presents polarization of each epoch for the full 2–8 keV range. The right-hand panel illustrates the energy dependence of these quantities. Most critically, while polarized X-rays are detected with high significance, they yield a markedly lower PD compared to the hard state (viz 2% versus 4%). For the soft-state data, the net 99% confidence minimum detectable polarization is 0.39%. The PD increases significantly with energy, as was also found in the hard state. The PA is constant over energy and in time (PA $\approx -26°$), just as seen for the hard

[70] The average disk fractions (by flux) for these soft states are $\approx$60% from 2 to 4 keV, $\lesssim$10% from 4 to 6 keV, and <1% above 6 keV.

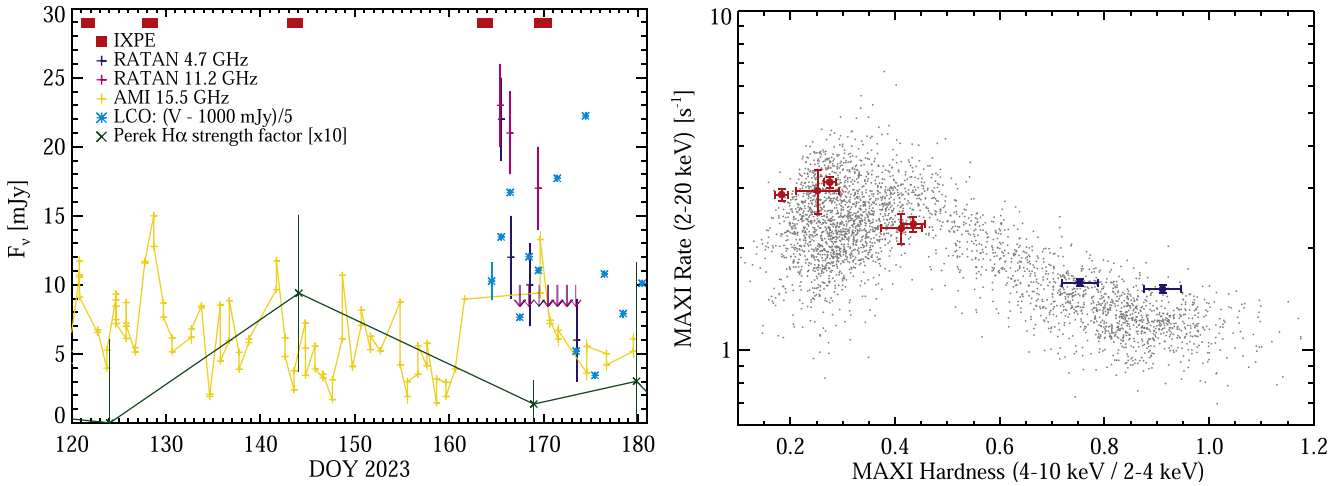

Figure 1. (Left) Cyg X-1 light curve in optical and radio over the span of the IXPE campaign (red bars). Radio data from AMI and RATAN reveal ongoing weak jet activity, with a potential flare near epoch 4. *V*-band optical data from LCO show structured variation at low amplitude ($\lesssim$10%), with emission dominated by the companion star. The same substructure also appears in the *B*, *r*′, and *i*′ bands (not shown here). Hα line strength factors from the Perek Telescope are shown in green. The larger time baseline of this monitoring reveals that a high line strength factor is associated with a decrease in X-ray and an increase in radio flux (increasing Hα in the companion's stellar wind). Light curves are in mJy unless otherwise indicated. (Right) MAXI hardness–intensity diagram of Cyg X-1, with the five IXPE soft-state epochs marked in red and the two hard states in blue.

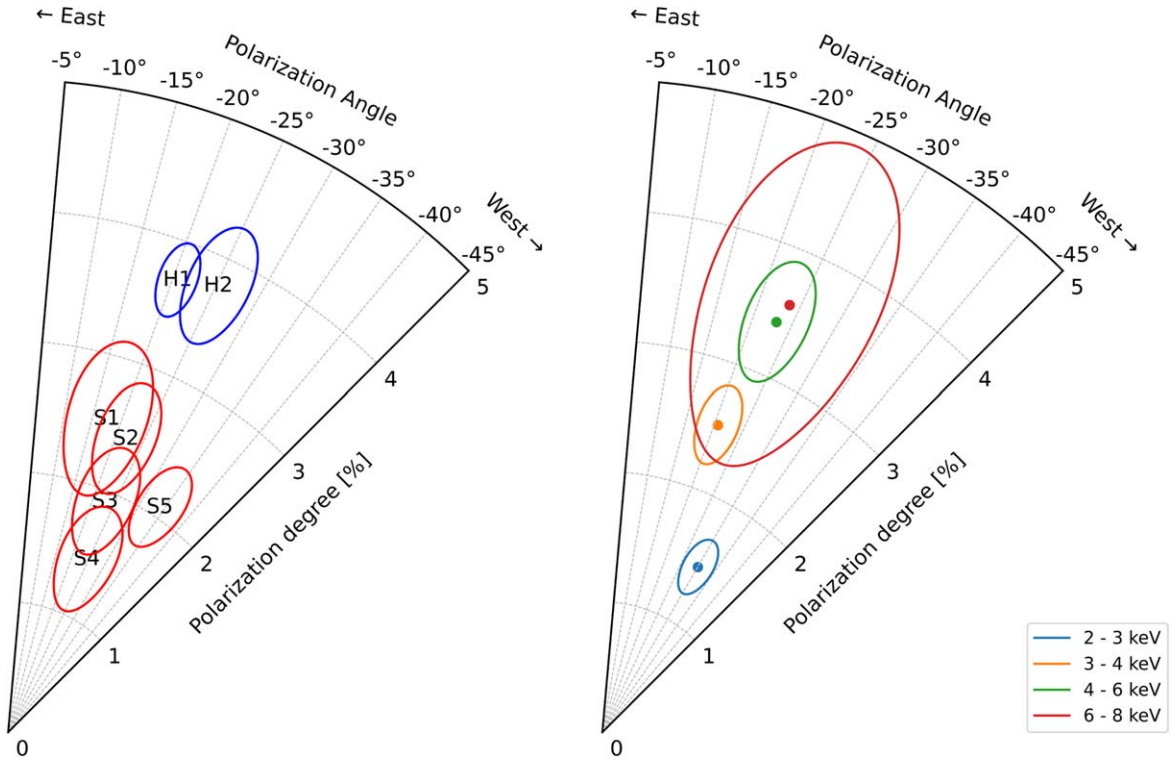

Figure 2. (Left) IXPE 2–8 keV PD and PA for each soft state (S1–S5; red) in comparison to previous hard-state observations (H1–H2; blue). (Right) Energy-dependent polarization of the soft-state data composite. Contours show 68% confidence intervals.

state (Krawczynski et al. 2022), and aligned to Cyg X-1's radio jet and radio lobes (Stirling et al. 2001).

3.2. Spectral Analysis

While coronal emission canonically dominates hard-state X-ray spectra of X-ray binaries, even in Cyg X-1's soft states, the coronal emission contributes appreciably to the X-ray signal. Because of this, reflection features, including the relativistically broadened Fe-Kα fluorescence line at $\sim$6.5 keV and a "Compton hump" at $\sim$30 keV, are correspondingly pronounced in the spectra. Accordingly, spectral models must contain both coronal and reflection components in addition to the thermal disk.

3.2.1. Phenomenological Model

An initial phenomenological spectral analysis of Cyg X-1 is first pursued using the model tbFeO ×(diskbb+smedge×nthcomp+laor). Here, tbFeO (Wilms et al. 2000) describes absorption by the interstellar medium while allowing for nonstandard Fe and O abundances. The multicolor disk emission is provided by diskbb and the coronal Compton emission by nthcomp (Zdziarski et al. 1996; Życki et al. 1999). Reflection is approximated by the combination of a smeared Fe edge (smedge; Ebisawa et al. 1994) and the inclusion of a broadened Fe line (laor; Laor 1991). We account for a tear in the thermal shielding of NuSTAR's FMPA via NuSTAR's nuMLIv1 model (Madsen et al. 2020).

This model has been applied separately for each epoch, and although it falls short in capturing the detailed reflection structure, most importantly, it reasonably fits the continuum. These empirical fits have χ^2/dof fit statistics of 3484.7/2767, 771.3/791, and 5126.6/3836 when fitting the data in Table 1 for epochs 3, 4, and 5, respectively. We find that the inner temperature of the diskbb component is 0.506 ± 0.003 keV for epoch 3, $0.479^{+0.004}_{-0.007}$ keV for epoch 4, and $0.492^{+0.003}_{-0.005}$ keV for epoch 5. Over the full IXPE band, the ratio of thermal (disk) to nonthermal (corona plus reflected) flux is 1.0, 0.82, and 0.58 for epochs 3, 4, and 5, respectively.

3.2.2. Fully Relativistic Model

We next employ a fully relativistic spectral model in which we replace diskbb with kerrbb (Li et al. 2005), replace nthcomp with the coronal scattering kernel simplcut (Steiner et al. 2009, 2017), and use relxillCP (Dauser et al. 2014; García et al. 2014) to produce reflection emission. Distant reflection from the companion star or a disk rim is included via xillverCp. In addition, wind absorption is incorporated using zxipcf (Reeves et al. 2008). The wind features are unconstrained without low-energy coverage, and so for epoch 4, we assume the absorption and wind parameters are the same as in epoch 5, which was similar in orbital phase. A spectral-hardening factor in kerrbb describes the ratio of color to effective temperature for the thermal disk. These are decoupled primarily as a result of strong electron scattering in the disk atmosphere. The factor was determined to be $f_{\rm col} = 1.55$ using the disk-atmosphere model bhspec (Davis & Hubeny 2006) for Cyg X-1's parameters at the temperature and luminosity of our observations, and so we adopt this value throughout. For kerrbb, we fix the BH mass to $21.2\,M_\odot$ and distance to 2.22 kpc (Miller-Jones et al. 2021) and assume that the disk is aligned with the binary inclination of $27^\circ.1$ (Orosz et al. 2011).[71] We note that parameter degeneracy within the continuum-fitting disk model prevents a reliable inclination fit for these data (e.g., Gou et al. 2011; Steiner et al. 2011). We apply kerrbb's returning radiation flag but not limb darkening given the strong irradiation in evidence.

The full model formulation is zxipcf × tbFeO × [simplcut (kerrbb + mbknpo × relxillCp) + mbknpo × xillverCp]. Here, mbknpo is used to curtail unphysical runaway in the reflection spectrum at energies near and below the thermal disk's peak. This runaway occurs because the reflection model has been computed for a seed disk temperature of $kT_* = 50$ eV. With mbknpo, we apply a break in the power-law shape of the reflection below a reference energy (typically several times the thermal disk peak). Below this energy, the shape is forced to follow the low-energy tail of a multicolor disk (as one expects, given the thermal disk photons that seed the Compton component).

The photon index Γ and electron temperatures $kT_{\rm e}$ of the reflection components are tied to corresponding settings in simplcut, which makes use of the nthcomp kernel. The xillverCp component is assumed to originate with low ionization ($\log \xi = 0$). In order to allow for potential systematic uncertainties in the reflection model while also exploring potential misalignment between the spin and orbital axes, we leave the inclination free in relxillCp (but not for kerrbb). For analogous reasons, the spin is decoupled between components.

Owing to their short duration and high signal-to-noise, each NICER good time interval (GTI) is fitted for mass accretion rate $\dot{m}$, coronal scattering fraction $f_{\rm sc}$, wind column $N_{\rm H}$, and reflection normalization. A single set of those values is fitted across the long-exposure spectra from IXPE, NuSTAR, and INTEGRAL. Each instrument is assigned a floating cross-normalization constant with respect to NuSTAR's FPMB. All other parameters are assumed to be invariant during an epoch. For the IXPE and AstroSat instruments, the instrumental gain and energy zero-points are included as free parameters of the fit. To account for instrumental residuals at Si–K in the NICER spectrum, we include a Gaussian absorption line at 1.74 keV with 5 eV width (Si Kα) and an edge at 1.84 keV.

Our comprehensive spectral fits are presented in Table 2 and illustrated for epoch 5 in Figure 3. Because each spectrum contains millions of counts, many spectral bins are limited by systematic uncertainty that can arise from deficiencies either in the instrument calibration or in the spectral model. Although the fit statistics obtained are formally unacceptable, an additional systematic uncertainty from 0.4% to 0.8% would result in a reduced χ^2 of unity for each epoch, which we find eminently reasonable given typical calibration uncertainties (see, e.g., Madsen et al. 2017). We note that the break energy of the mbkpno reflection modifier is higher than might be expected for a disk with $kT_* \approx 0.5$ keV, which we tentatively attribute to a large gravitational redshift for this high-spin BH. We additionally note that the inclination from the reflection modeling differs substantially among the epochs, with $i \approx 30^\circ$ for epochs 4 and 5 in agreement with the binary orbital inclination from Orosz et al. (2011), whereas the higher inclination $i \approx 40^\circ$ from epoch 3 more closely matches that obtained in Krawczynski et al. (2022). The BH spins we find are all high. The continuum-fitting spin value is maximal for each fit, whereas the reflection spin is consistently high ($\gtrsim$0.9) but exhibits variance larger than the statistical uncertainty. We attribute these differences to systematic uncertainties in the model. We note that if disk and reflection inclinations are linked, the inclination is driven to the disk value in epochs 3 and 5. This linking does not have a significant impact on the other model parameters but produces a significantly worse fit.

For epochs 3 and 5 (those with soft X-ray coverage), the fit was found to improve when including an additional thermal component, which fits with a temperature of ∼1–1.5 keV and a flux of ∼10% of the primary thermal component. We speculate that such a component may originate from thermalized reflection returning radiation at the disk surface. However,

[71] The disk rotates clockwise, which then corresponds to $i_{\rm orb} = 153^\circ$, though in this work, we will simply adopt a 0°–90° range convention referring to the inclination magnitude.

Table 2
X-Ray Spectral Fits

Component	Variable	Unit	Epoch 3	Epoch 4	Epoch 5
TBfeo	$N_{\rm H}$	10^{22} cm^{-2}	$0.7501^{+0.0021}_{-0.0005}$	0.75 (f)	$0.7487^{+0.0009}_{-0.0008}$
	O		$1.072^{+0.005}_{-0.003}$	1.08 (f)	$1.080^{+0.004}_{-0.002}$
	Fe		0.46 ± 0.02	0.42 (f)	0.41 ± 0.02
zxipcf	$N_{\rm H}$	10^{22} cm^{-2}	2.76 (t)	3.03 (f)	3.21 (t)
	$\log \xi$		2.30 ± 0.02	2.10 (f)	2.07 ± 0.02
	CvrFract		$0.258^{+0.006}_{-0.011}$	0.22 (f)	$0.246^{+0.010}_{-0.007}$
simplcut	Γ		$1.988^{+0.002}_{-0.003}$	$2.090^{+0.009}_{-0.005}$	$2.090^{+0.004}_{-0.002}$
	$f_{\rm sc}$		$0.0384^{+0.0027}_{-0.0007}$	$0.057^{+0.003}_{-0.002}$	0.076 ± 0.002
	$kT_{\rm e}$[a]	keV	$500^{(p)}_{-140}$	$500^{(p)}_{-110}$	$500^{(p)}_{-120}$
mbkpno	B	keV	$3.87^{+0.05}_{-0.03}$	$3.80^{+0.07}_{-0.05}$	2.55 ± 0.04
relxillCP	i	deg	32.7 ± 0.6	30.7 ± 1.2	29.1 ± 0.4
	a_*		$0.931^{+0.015}_{-0.004}$	$0.89^{+0.07}_{-0.04}$	$0.925^{+0.003}_{-0.005}$
	Rbr	$r_{\rm G}$	$4.03^{+0.08}_{-0.17}$	$7.9^{+1.6}_{-1.2}$	$3.90^{+0.06}_{-0.08}$
	Index1		$6.6^{+0.1}_{-0.1}$	5.0 ± 0.3	$7.5^{+0.1}_{-0.2}$
	Index2		$3.13^{+0.02}_{-0.03}$	$2.5^{+0.1}_{-0.3}$	$2.905^{+0.013}_{-0.014}$
	$\log \xi$		$3.341^{+0.004}_{-0.015}$	$3.81^{+0.05}_{-0.04}$	$3.646^{+0.014}_{-0.015}$
	logN	cm^{-3}	$19.99^{+0.01(p)}_{-0.05}$	$18.6^{+0.2}_{-0.1}$	$18.58^{+0.17}_{-0.05}$
	Afe		$10.00^{(p)}_{-0.07}$	$10.0^{(p)}_{-0.3}$	$10.0^{(p)}_{-0.3}$
	norm		0.0195 ± 0.0003	$0.029^{+0.001}_{-0.002}$	$0.0437^{+0.0007}_{-0.0008}$
kerrbb	a_*[b]		$0.99964^{+0.00007}_{-0.00003}$	$0.9999^{(p)}_{-0.0003}$	$0.99990^{(p)}_{-0.00004}$
	$\dot{M}$	10^{18} g s^{-1}	0.245 ± 0.002	$0.201^{+0.002}_{-0.001}$	$0.2183^{+0.0008}_{-0.0005}$
	$f_{\rm col}$		1.55 (f)	1.55 (f)	1.55 (f)
xillverCP	logN	cm^{-3}	$16.0^{+1.1}_{-0.2}$	$15.2^{+0.8}_{-0.2(p)}$	$15.98^{+0.06}_{-0.24}$
	norm		$0.0032^{+0.0001}_{-0.0003}$	$0.0045^{+0.0009}_{-0.0005}$	$0.0045^{+0.0004}_{-0.0003}$
NuSTAR/FPMA	Constant		1.008 ± 0.002	1.005 ± 0.002	1.014 ± 0.002
MLI	covfrac		$0.82^{+0.01}_{-0.01}$	0.81 ± 0.02	$0.826^{+0.010}_{-0.006}$
INTEGRAL/IBIS	Constant		…	1.16 ± 0.02	$1.528^{+0.014}_{-0.013}$
AstroSat/SXT	Constant		0.890 ± 0.006	…	…
	Gain fit slope		$1.033^{+0.003}_{-0.002}$	…	…
	Gain fit offset		$0.011^{+0.007}_{-0.006}$	…	…
AstroSat/LAXPC	Constant		$0.88^{+0.02}_{-0.03}$	…	…
	Gain fit slope		0.99 ± 0.02	…	…
	Gain fit offset		$-0.05^{+0.09}_{-0.07}$	…	…
IXPE/DU1	Constant		0.847 ± 0.005	$0.867^{+0.008}_{-0.010}$	$0.912^{+0.007}_{-0.009}$
	Gain fit slope		0.961 ± 0.002	$1.022^{+0.004}_{-0.002}$	1.045 ± 0.002
	Gain fit offset		$0.0314^{+0.008}_{-0.009}$	$-0.107^{+0.010}_{-0.006}$	-0.157 ± 0.009
IXPE/DU2	Constant		$0.815^{+0.007}_{-0.005}$	$0.845^{+0.007}_{-0.009}$	0.875 ± 0.008
	Gain fit slope		$0.9700^{+0.0015}_{-0.0016}$	$0.981^{+0.003}_{-0.002}$	1.032 ± 0.002
	Gain fit offset		$0.049^{+0.007}_{-0.008}$	$-0.005^{+0.010}_{-0.012}$	-0.109 ± 0.009
IXPE/DU3	Constant		$0.775^{+0.006}_{-0.005}$	$0.803^{+0.006}_{-0.008}$	$0.838^{+0.007}_{-0.004}$
	Gain fit slope		…	$1.001^{+0.003}_{-0.002}$	1.031 ± 0.002
	Gain fit offset		…	$-0.014^{+0.010}_{-0.011}$	-0.096 ± 0.009
NICER	Constant		1.0 (f)	…	1.0 (f)
	Strength (1.74 keV)		$-0.0022^{+0.0002}_{-0.0004}$	…	-0.0010 ± 0.0003
	MaxTau (1.84 keV)		$0.039^{+0.002}_{-0.003}$	…	$0.047^{+0.002}_{-0.001}$
	Wind $N_{\rm H}$[c]	10^{22} cm^{-2}	1.88–4.73	…	1.48–5.51
	$f_{\rm sc}$[c]		0.037–0.051	…	0.076–0.139
	Relative reflection[c]		0.77–1.12	…	0.79–1.25
	$\dot{M}$[c]	10^{18} g s^{-1}	0.258–0.280	…	0.220–0.266
FIT STATISTIC	χ^2/dof		3532.39/2740	896.67/783	4133.97/3799

Notes. Best fit and 90% confidence intervals for our preferred fully relativistic model applied to epochs 3, 4, and 5. Parameters with (t) are tied to others, as described in the text, while those marked (f) are fixed due to a lack of low-energy spectral coverage in epoch 4. Any value pegged at a hard limit is marked (p). Relative reflection describes a per-GTI scale factor for both reflection components.

[a] At such high electron temperatures, the diffusion approximation built into the nthcomp model is insufficient, which may account for residuals at $\gtrsim$50 keV in Figure 3. While not included in our model, those residuals can be well fitted using an ad hoc broad Gaussian with negligible impact on the other fit parameters.

[b] The spin uncertainty is adopting a fixed M, i, and D and does not include measurement uncertainty from those terms or any model systematic uncertainty.

[c] Parameters are left to vary in each NICER GTI; ranges shown depict the GTI ensemble.

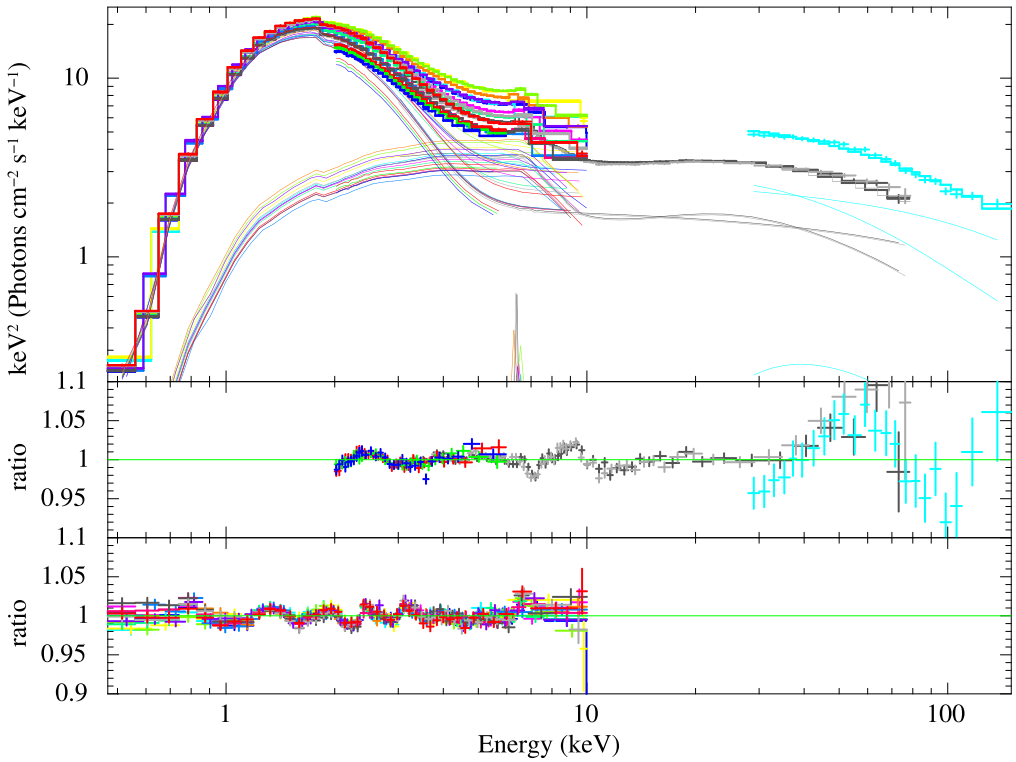

Figure 3. The best-fitting comprehensive spectral model for epoch 5, showing contributions from the Comptonized disk and reflection components. Each NICER GTI contains 5–30 million counts; the IXPE, NuSTAR, and INTEGRAL spectra contain ∼2–4 million counts apiece. For clarity, the ratios of data to best-fit model are split between the lower two panels. The middle panel shows NuSTAR FMPA (dark gray) and FMPB (light gray); IXPE DU1 (red), DU2 (green), and DU3 (blue); and INTEGRAL IBIS (cyan). The lower panel shows the ratio of the spectra from the different NICER GTIs. The same color scheme is used for the unfolded data sets and model in the upper panel.

because other modeling systematics are of comparable magnitude, we opt against including this additional component in our adopted model.

3.3. Empirical Polarimetric Fitting

We fix the best-fitting spectral (and response-model) parameters and, for each epoch, attempt to fit the IXPE Stokes Q and U data, testing each of the three spectral components separately: (i) the transmitted disk spectrum, (ii) the transmitted reflection spectrum, and (iii) the total Compton upscattered spectrum. Each component is assigned a constant PD and PA (`polconst`), and we assess which component(s) are capable of producing the observed signal. In each case, the disk emission is insufficient, owing to its negligible contribution to high energies in particular. Instead, either of the reflection or coronal components are capable of accounting for the observed signal. Because the reflection signal is dominant over the coronal component, it need not be as highly polarized. Using just the Stokes data from IXPE, it is not possible to distinguish polarimetric contributions between the coronal and reflection components, which are similarly shaped over the 2–8 keV range. The observed polarization cannot empirically distinguish between the two components, and so a more detailed physical investigation is required, which we present in Section 4. Here, for this empirical analysis, we consider alternate cases in which the polarization is solely attributed to one or the other component.

At 90% confidence intervals for our preferred fits, for polarization to arise solely from the coronal component in epochs 3, 4, and 5 would require $\mathrm{PD} = 17.8\% \pm 3.3\%$, $8.0\% \pm 3.6\%$, and $7.8\% \pm 2.4\%$, respectively. The corresponding PAs are $-16^\circ \pm 5^\circ$, $-25^\circ \pm 13^\circ$, and $-26^\circ \pm 9^\circ$. If the polarization is instead attributed solely to reflection emission, the required $\mathrm{PD} = 10.9\% \pm 2.0\%$, $4.3\% \pm 1.9\%$, and $5.2\% \pm 1.6\%$, respectively; the corresponding PAs are $-16^\circ \pm 5^\circ$, $-26^\circ \pm 13^\circ$, and $-26^\circ \pm 9^\circ$. We find that epochs 4 and 5 are each marginally improved by allowing polarization of the disk emission, although the improvement is insignificant for epoch 3. For epochs 4 and 5, the disk offers a marginal PD of $1.3\% \pm 1.0\%$ and $1.3\% \pm 1.0\%$, with PAs of $-2^\circ \pm 25^\circ$ and $-36^\circ \pm 26^\circ$, respectively.

Absent broadband X-ray spectral data for epochs 1 and 2, we perform a simple analysis of these using a disk-plus-power-law model for the IXPE data alone. At 90% confidence, in epochs 1 and 2, the power-law component has $\mathrm{PD} = 4.6\% \pm 1.2\%$, $4.5\% \pm 0.7\%$ and $\mathrm{PA} = -22^\circ \pm 8^\circ$, $-21^\circ \pm 4^\circ$, respectively. The disk component has insignificant polarization in epoch 2 but is marginally detected in epoch 1 with $\mathrm{PD} = 3.2\% \pm 3.0\%$ and $\mathrm{PA} = 53^\circ \pm 37^\circ$.

4. Discussion

Cyg X-1's soft-state polarization properties are similar to those seen in other recent IXPE observations of soft and SPL states, including 4U 1630−47 (Rodriguez Cavero et al. 2023; Ratheesh et al. 2024), LMC X-1 (Podgorný et al. 2023), 4U 1957+11 (Marra et al. 2024), LMC X-3 (Svoboda et al. 2024a), and Swift J1727.8−1613 (Svoboda et al. 2024b). 4U 1957+11 in particular shows similarly strong returning radiation as here, and in each system with sufficient signal, the PD increases with energy while the PA remains approximately

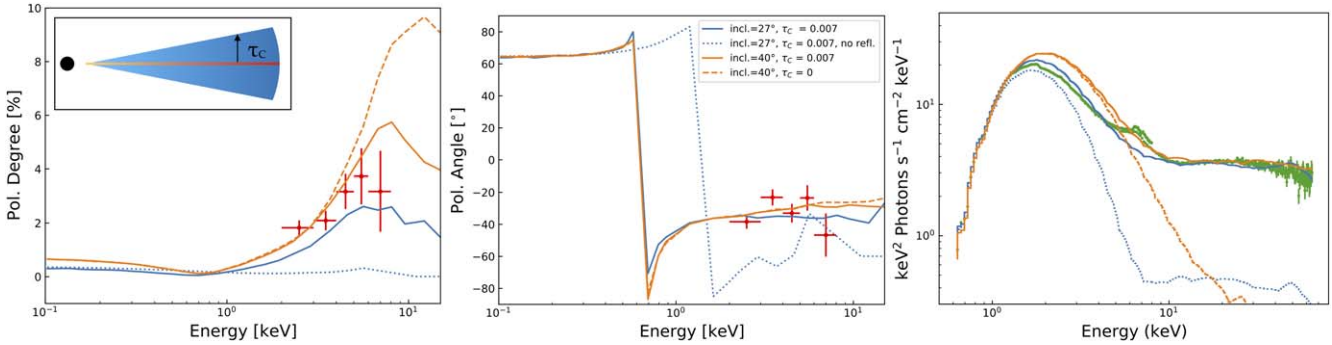

Figure 4. kerrC simulations of the PD (left), PA (middle), and spectrum (right) expected from a standard geometrically thin, optically thick accretion disk of a rapidly spinning BH ($a_* = 0.998$) with a hot wedge-shaped corona (illustrated in the left panel inset). We show results for inclinations of $i = 27°$ (close to the orbital inclination; blue lines) and a higher inclination of $i = 40°$ (orange lines). We furthermore demonstrate the effect of removing the corona but not the returning emission (dashed orange line) and of removing all reflected emission (blue dotted line). The polarization signal is clearly dominated by the reflected emission. The IXPE polarization data for epoch 5 (red data points) support high spin, owing to the impact of the reflected emission. Note the polarization swing at ∼0.5 keV for all models with disk reflection. Very similar results are obtained for epochs 3 and 4. Green points in the right panel depict the NICER and NuSTAR data.

fixed, in contrast to the classical expectation of large swings in PA and PD above the thermal peak for a BH with an electron-scattering disk atmosphere (Connors et al. 1980; Dovčiak et al. 2008; Schnittman & Krolik 2009, 2010).

We investigated Cyg X-1's spectropolarization properties using the general relativistic ray-tracing code kerrC (Krawczynski & Beheshtipour 2022; Krawczynski et al. 2022), adopting a wedge-shaped corona corotating with the accretion disk (see Poutanen et al. 2023 and Dexter & Begelman 2024 for an alternative explanation involving relativistic outflows). The kerrC code assumes a razor-thin accretion disk extending from the ISCO to 100 gravitational radii $r_g = GM/c^2$. In kerrC, the disk emits radiation polarized according to Chandrasekhar's classical results for a semi-infinite scattering atmosphere accounting for the reflection to all scattering orders (Chandrasekhar 1960, Equation (164) and Table 10XV); see Krawczynski (2012) and Krawczynski & Beheshtipour (2022) for more details. kerrC can modulate the intensity of the reflected emission according to reflection radiative transport codes (García et al. 2014, and references therein); however, we switch off that expensive capability here, owing to the high ionization of the disk.

As in the hard-state analysis from Krawczynski et al. (2022), we use a wedge-shaped corona extending from $r_{\rm ISCO}$ to a fixed $100\,r_g$ with a fixed half-opening angle of 10°. We use a modified version of kerrC that implements a corona orbiting the symmetry axis at the position (r, θ, ϕ) (Boyer–Lindquist coordinates) with the Keplerian angular velocity evaluated in the equatorial plane at the radial coordinate $r_D = \sin\theta r$. In the original kerrC model, the corona orbits the symmetry axis with the zero angular momentum observer (ZAMO) angular frequency. We find that the Kepler and ZAMO coronae give very similar flux and polarization energy spectra. kerrC assumes a single temperature and vertical optical depth τ_C for the entire corona (see the sketch in Figure 4). kerrC assumes a 3D corona geometry, so the effective optical depth varies spatially. Note that perfect reflection off the disk increases the coronal flux at high energies substantially as photons back-scattered by the corona in the direction of the disk gain more energy than photons forward-scattered in the direction of the observer. The disk can reflect these higher-energy photons toward the observer. The reflecting disk furthermore increases the effective optical depth (see also Haardt 1993). The polarization change in coronal scatterings is effected in the electron rest frame using Fano's relativistic scattering matrix (Fano 1957; Beheshtipour et al. 2017).

We fixed the BH mass, distance, spin, and accretion rate to the kerrbb values assumed or fitted in Table 2. We tested the binary orbital inclination, the reflection inclinations from Table 2, and several other reference values. The vertical coronal optical depth τ_C (∼0.007 for epoch 5) and the corona electron temperature kT_e (∼250 keV) were obtained from an eyeball fit of the NICER and NuSTAR spectral data. The vertical coronal optical depth for epoch 5 was significantly larger than for epochs 3 or 4 ($\tau_C \sim 0.002$), in line with the trend of f_{sc} in the spectral fits. A comparison between the kerrC polarization prediction and the IXPE data is displayed in Figure 4. We find that for kerrC to match the high PD values observed, high spins of $a_* \gtrsim 0.96$ are required. At these high spins, the inner edge of the disk is very close to the event horizon; so, due to gravitational lensing from the strong spacetime curvature, a large fraction of photons, both thermal and reflection, return to the disk (e.g., Dauser et al. 2022). The latter is most important at the higher energies in IXPE's bandpass. These reflect off the disk and generate high PDs (Schnittman & Krolik 2009; Taverna et al. 2020; Krawczynski & Beheshtipour 2022). The PDs are slightly underpredicted for an inclination of $i = 27°$ and slightly overpredicted for $i = 40°$. For the $i = 27°$ model, the blue dotted line shows the result when reflection photons are omitted, and the resulting deficit in polarization highlights the large contribution from these reflected photons. The orange dashed line shows the impact of removing the corona from the $i = 40°$ model. Here, the disk with its reflected returning radiation produces even an higher PD than from the disk–corona model. The high polarization for this case was verified using kynbbrr (Taverna et al. 2020). Additional exploration with kerrC reveals that the net PD and PA values are insensitive to the coronal temperature kT_e, as reflection dominates the polarization signature. We note that Fe-Kα emission is expected to reduce the PD in the 6–8 keV energy band. The effect on the PD is, however, 1 order of magnitude smaller than the IXPE measurement error.

We separately investigated predictions for the disk-plus-slab corona model using the polarimetric Comptonization code compps (Poutanen & Svensson 1996; Veledina & Poutanen 2022). Ray tracing was performed with the code ARTPOL based on analytical results (Loktev et al. 2022, 2024). A slab geometry was adopted with $\tau = 0.2$ to match the slope of the

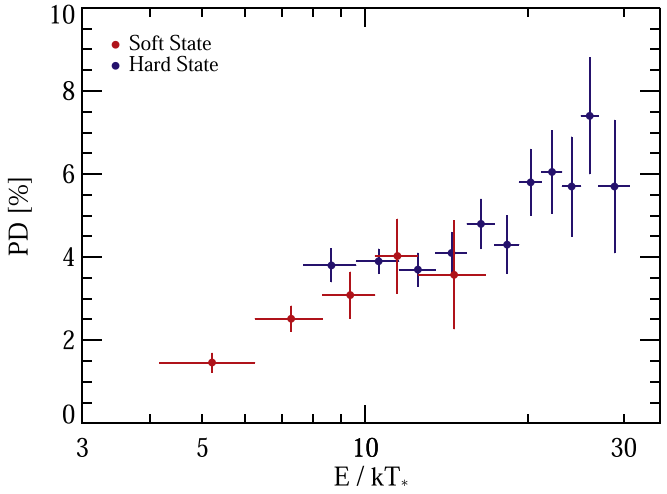

Figure 5. IXPE PD for the composite of hard vs. soft states, where the energy bins have been scaled with respect to the disk temperature kT_*. The consistent behavior in evidence is suggestive of commonality between the hard and soft states, despite radically different spectral-timing characteristics.

power law observed at high energies. A purely Maxwellian electron distribution with $kT_e = 92$ keV was adopted and the spin set to the maximum value allowed by ARTPOL ($a_* = 0.94$). The associated Compton-component polarization was very low. Specifically, the predicted PDs are substantially lower than the observed values for inclinations between 30° and 45° (e.g., <1% in the IXPE bandpass at $i = 30°$).

In `kerrC` and `kynbbrr`, the transition from dominance of direct emission to reflection emission produces a ∼90° PA swing around 0.5 keV, whereas absent reflection, from Comptonization in the corona, such a swing would occur at near 5 keV energy in the transition from the disk-dominated to the corona-dominated energy band. As can be seen in Figure 4, when reflection is omitted from `kerrC`, the predicted the Compton-component polarization is very low, in good agreement with the `compps` results. Higher PDs could be generated by combining lower electron temperatures with higher optical depths (e.g., Sunyaev & Titarchuk 1985) or with a hybrid (thermal and nonthermal) electron distribution (Gierliński et al. 1999), with nonthermal electrons expected to dominate the Comptonization tail at the highest energies.

In Cyg X-1's IXPE+NICER+NuSTAR hard-state analysis by Krawczynski et al. (2022), the PA was measured to be stable with energy and in alignment with both the radio-jet orientation and the intrinsic PA in the optical (Kravtsov et al. 2023). At the same time, the PD was found to increase approximately linearly with energy in the best fit, much as here.

Figure 5 shows an intriguing trend of the PD increasing with the energy in units of its natural scale, the disk's temperature. In the soft state, our best model attributes the PD increase with energy to the growing dominance of returning-radiation-induced reflection. The hard-state fit was explained as PD rising owing to the increasing number of scatterings experienced by higher-energy photons. The appearance of a common trend produced by the hard- and soft-state PD energy spectra is intriguing, although we note that it may simply be coincidental.

5. Conclusions

We present the first IXPE polarimetric observations of Cyg X-1's soft state. The soft state exhibits weaker polarization (PD ≈ 2%) compared to the hard state, but in every other respect, the polarimetric properties of both states are strikingly similar, including a constant PA ≈ −26° (a direction parallel to Cyg X-1's jet) and a rising PD with energy. This commonality is bolstered by their adherence to a single track of PD versus energy when normalizing the IXPE energy bins by the observed disk temperature (Figure 5). At the same time, our best model attributes the polarization signatures in the hard and soft states to different dominant effects. Whereas in the IXPE band, hard-state polarization was explained as originating from multiply scattered photons in the corona, the soft-state polarization is explained as the result of returning radiation associated with the reflection emission, a consequence of the high spin and strong gravitational lensing for the inner disk.

In addition to the polarimetric analysis, accompanying multi-wavelength data in the radio, optical, and X-ray are also presented. Broadband X-ray spectral data span ∼0.5−500 keV. The associated spectral fits use tens of millions of counts, anchoring the thermal disk, coronal, and reflection contributions. Spectro-polarimetric modeling of these data with the wedge-shaped coronal geometry used to fit the hard state (with `kerrC`) also proved successful at describing the soft state as well. The polarimetric results constrain a high spin ($a_* \gtrsim 0.96$) and allow up to a $\lesssim$10° more inclined spin axis compared to the binary orbit.

Acknowledgments

The Imaging X-ray Polarimetry Explorer (IXPE) is a joint US and Italian mission. The US contribution is supported by the National Aeronautics and Space Administration (NASA) and led and managed by its Marshall Space Flight Center (MSFC), with industry partner Ball Aerospace (contract NNM15AA18C). The Italian contribution is supported by the Italian Space Agency (Agenzia Spaziale Italiana, ASI) through contract ASI-OHBI-2022-13-I.0, agreements ASI-INAF-2022-19-HH.0 and ASI-INFN-2017.13-H0, and its Space Science Data Center (SSDC) with agreements ASI-INAF-2022-14-HH.0 and ASI-INFN 2021-43-HH.0, and by the Istituto Nazionale di Astrofisica (INAF) and the Istituto Nazionale di Fisica Nucleare (INFN) in Italy. This research used data products provided by the IXPE Team (MSFC, SSDC, INAF, and INFN) and distributed with additional software tools by the High-Energy Astrophysics Science Archive Research Center (HEASARC) at NASA Goddard Space Flight Center (GSFC).

Some of the radio data were obtained at RATAN-600 SAO RAS, with the data processing supported by the Ministry of Science and Higher Education of the Russian Federation grant No. 075-15-2022-262 (13.MNPMU.21.0003). This work makes use of data from the AstroSat mission of the Indian Space Research Organisation (ISRO), archived at the Indian Space Science Data Centre (ISSDC). The article has used data from the SXT and the LAXPC developed at TIFR, Mumbai, and the AstroSat POCs at TIFR are thanked for verifying and releasing the data via the ISSDC data archive and providing the necessary software tools. The results presented include work supported by Tamkeen under the NYU Abu Dhabi Research Institute grant CASS.

J.F.S. acknowledges support from NASA contract NAS8-03060 and NuSTAR General Observer Program 80NSSC 23K1660. E.N. acknowledges support from NASA theory grant 80NSSC20K0540. M.D., J.S., J.Pod., and V.Kar. thank GACR project 21-06825X for the support and institutional support from RVO:67985815. A.V. thanks the Academy of Finland grant 355672 for support. A.A.Z. acknowledges support from the Polish National Science Center grant 2019/35/B/ST9/03944. P.-O.P. and M.P. acknowledge support from the High Energy National Programme (PNHE) of Centre national de la recherche scientifique (CNRS) and from the French space agency (CNES). I.L. was supported by the NASA Postdoctoral Program at the Marshall Space Flight Center, administered by Oak Ridge Associated Universities under contract with NASA. F.Mu., E.Co., A.D.M., R.F., P.So., S.F., and F.L.M. are partially supported by MAECI with grant CN24GR08 "GRBAXP: Guangxi-Rome Bilateral Agreement for X-ray Polarimetry in Astrophysics." We thank the anonymous referee for the stimulating feedback on our investigation.

Facilities: IXPE, NuSTAR, NICER, AstroSat, INTEGRAL, RATAN, AMI, LCO, Perek Telescope.

Software: ixpeobssim, heasoft.

Appendix
Data Description

A.1. IXPE

IXPE epochs 1–5 correspond to IXPE observation IDs 02008201, 02008301, 02008401, 02008501, and 02008601, respectively. During these observations of Cyg X-1, owing to the source brightness, one detector (DU3) exhibited an excess of events at high energies, resulting in a hard tail. Such events are induced by instances of residual charge in the detector's region of interest producing unphysical tracks. These events have a signature similar to those of background events and so can be removed by background screening; see Di Marco et al. (2023) for a complete discussion. These were correspondingly removed via background screening using the `filter_background.py` software.[72]

From cleaned level 2 event data for each gas pixel detector (GPD), 80″ and 60″ apertures were used to extract source data for polarimetric and spectroscopic analysis, respectively, using the `ixpeobssim` software suite (Baldini et al. 2022). A background region was extracted from an annulus with inner and outer radii of 150″ and 310″, centered on the source position. Data were extracted into "polarization cube" structures, allowing ready data slicing by detector, time, energy, etc.

We cross-checked these extractions by performing a standard analysis using XSELECT, using the effective event-number weighting (STOKES = "NEFF") to produce equivalent products in Stokes I, Q, and U parameters. In both instances, standard weighting with track ellipticity scaled to the 0.75 power was adopted, and the corresponding response files (v2 of the rmf and v5 of the arf) were used. Exposure times were corrected for $\lesssim$20% detector dead time. The IXPE Stokes Q and U data were analyzed in the 2–8 keV range, while the Stokes I data were analyzed in the 2–6 keV range due to flux calibration uncertainty.

[72] https://github.com/aledimarco/IXPE-background

A.2. NuSTAR

NuSTAR (Harrison et al. 2013) observed Cyg X-1 during each of epochs 3, 4, and 5 (observation IDs 80902318002, 80902318004, and 80902318006, respectively). A portion of the data collected during the latter two epochs was never relayed owing to problems with ground station contacts ($\sim$5.5 ks for epoch 4 and $\sim$3.5 ks for epoch 5). Cyg X-1 was sufficiently bright that those data were overwritten on board and were not recoverable. The three observations yielded exposure time of 13.8, 9.5, and 10.5 ks, respectively. Each observation was reduced following standard procedures for bright sources, including the modified NUFILTER condition "STATUS==b0000xxx00xxxx000" for producing clean level 2 data. Source events were extracted from a 100″ radius region centered on the source peak in each focal plane module (FPM), and in each case the background was obtained from a box of 750″ × 120″ at the detector edge. The spectral data were optimally binned via FTGROUPPHA (Kaastra & Bleeker 2016), dead-time-corrected, and analyzed from 3 to 79 keV. As the result of a tear in the FPMA thermal blanket (Madsen et al. 2020), following the guidance of the NuSTAR help desk, spectral analysis made use of the empirical correction table `NuMLIv1.mod`, which was used to adjust only FPMA, in order to account for its impact on the low-energy response.

A.3. NICER

NICER (Gendreau et al. 2012) observed Cyg X-1 during epochs 3 (observation IDs 6643010101 and 6643010102; eight useful GTIs in total) and 5 (observation IDs 6643010103 and 6643010104; 13 useful GTIs in total). GTIs were of typical duration, $\sim$1 ks, and were generally separated by one orbit of the International Space Station ($\sim$90 minutes) but sometimes separated by multiple orbits. All of these observations took place after the discovery of an optical light leak[73] caused by a damaged thermal shield on one of the detectors. During ISS daytime, the leak contributes additional noise at low energies and also can produce telemetry saturation from detector reset events. The daytime data were found to suffer significant packet losses, so the data were screened to select only dark conditions (filter setting "sunshine==0"). Aside from this requirement, the data were subject to standard level 2 processing and filtering using NICERDAS-v10 and extracted per continuous GTI. Any GTI less than 60 s was discarded. A total of 6.8 ks and 14.5 ks were produced for the two epochs in 8 and 13 GTIs, respectively (Table 1). For each GTI, individual detector behavior was screened against the instrument ensemble for each of undershoot (reset) event rates, overshoot (particle) event rates, and X-ray event rates, with any 10σ equivalent outlier detector flagged and excised from the ensemble. FPM 63 was flagged and removed in this way owing to an excess undershoot rate, which was seen in all GTIs. FPM 55 had been turned off during observations. The remaining 50 detectors were combined for all subsequent analysis. The NICER count rate varied between 20,000 and 24,000 s^{-1} (52 FPM equivalent), approximately twice the rate of the Crab. We computed backgrounds for each NICER GTI using the mission-recommended `scorpeon`[74] and 3C50 (Remillard et al. 2022) background models. These were

[73] https://www.nasa.gov/feature/goddard/2023/nicer-status-update

[74] https://heasarc.gsfc.nasa.gov/docs/nicer/analysis_threads/scorpeon-xspec/

negligible in comparison with the data in each case, and the background models were in close agreement. The exposure times were adjusted for ∼1% detector dead time. NICER spectral data were binned to oversample the detector energy resolution by a factor of ∼2 and analyzed over the range 0.5–11 keV with a 1% systematic error included.

A.4. INTEGRAL

INTEGRAL observed Cyg X-1 during epochs 4 and 5, from 2023 June 13 22:15:42.865 UTC to 2023 June 15 14:51:31.971 UTC (INTEGRAL revolution 2651) and from 2023 June 20 00:00:09.268 UTC to 2023 June 20 15:04:10.319 UTC (INTEGRAL revolution 2653). We consider all INTEGRAL individual pointings or science windows (scws) during these two periods. To probe the source behavior in the hard X-rays, we make use of data from the first detector layer of the Imager on Board the INTEGRAL Satellite (IBIS) and ISGRI, which is sensitive between ∼20 and ∼600 keV (Lebrun et al. 2003). Data were reduced with version 11.1 of the Off-line Scientific Analysis (OSA) software following standard procedures.[75] For each scw, a sky model was constructed, and the sky image and source count rates were reconstructed by deconvolving the shadowgrams projected onto the detector plane. Spectra were extracted using 40 logarithmically spaced channels between 20 and 1000 keV. Response matrixes were automatically generated running the OSA 11.1 spectral extraction. Subsequently, the `spe_pick` tool was employed to create stacked spectra for each distinct epoch, with the addition of a 2% systematic uncertainty, in accordance with the specifications outlined in the IBIS user manual. During the spectral fitting, a hard feature at $\gtrsim$200 keV dominated the flux. As this component was sufficiently far from the IXPE band of interest, we assume that this feature does not significantly affect the spectrum at lower energies; thus, the spectral fits presented in Section 3 only considered the INTEGRAL data below 150 keV.

A.5. AstroSat

AstroSat (Singh et al. 2014) observed Cyg X-1 during epoch 3 from 2023 May 24 19:11:50 UT to 2023 May 25 11:55:00 UT (observation ID T05_105T01_9000005662). The primary instrument for the observation was the Soft X-ray Telescope (SXT; Singh et al. 2016, 2017) operating in fast window mode. The Large Area X-ray Proportional Counter (LAXPC; Yadav et al. 2016, 2017) also observed the source simultaneously in event analysis mode.

We procured the level 2 data for SXT (as processed by the Payload Operation Centre, POC) and extracted standard products (i.e., light curve and spectra) for individual AstroSat orbits using XSELECT. We used an annular region with an inner radius of 3′ and outer radius of 5′ to mitigate pileup effects in the extracted products. The spectra were extracted for individual AstroSat orbits and merged via ADDSPEC. We used standard response and background files provided by the SXT POC and modified the ancillary response file to correct for the annular region adopted. For spectral modeling, we fit the energy range 0.8–7.0 keV (Bhargava et al. 2023) and adopt a 3% systematic error.

LAXPC level 1 data were processed using LAXPCSOFTWARE22AUG15 (Antia et al. 2021; Misra et al. 2021). We obtain the spectrum, light curve, background spectrum, and responses using pipeline tools. LAXPC data are fitted from 3 to 35 keV, beyond which the spectrum is background-dominated. We include a 3% systematic error in our analysis to mitigate residual uncertainties in the response (Bhargava et al. 2022). We use data from only one proportional counter unit (LAXPC20; Antia et al. 2021), as LAXPC30 ceased operation early in the mission due to gas leakage, and LAXPC10 has presented abnormal gain variations.

A.6. LCO

Optical monitoring of Cyg X-1 was performed with the LCO 1 m robotic telescopes located in McDonald Observatory (Texas, USA) and with the Teide Observatory (Tenerife, Spain) from 2023 June 2 (MJD 60097.34) to 2023 July 2 (MJD 60127.93), using B, V, r', and i' filters. Due to the brightness of the source, all the observations had 2 s exposure times to avoid saturating the instrument. The acquired images were processed and analyzed by the XB-NEWS pipeline (see Russell et al. 2019 and Goodwin et al. 2020), carrying out the following tasks.

1. Download fully reduced images from the LCO database (i.e., bias-, dark-, and flat-field-corrected images).
2. Reject any images of poor quality.
3. Perform astrometry using Gaia DR2 positions.
4. Carry out multiaperture photometry (MAP; Stetson 1990).
5. Solve for photometric zero-point offsets between epochs (Bramich & Freudling 2012).
6. Flux-calibrate the photometry using the ATLAS-REFCAT2 catalog (Tonry et al. 2018).

If the target is not detected in an image above the defined detection threshold (a very unlikely prospect for Cyg X-1), XB-NEWS performs forced MAP at the target coordinates. If forced MAP was performed, we reject any with an uncertainty above 0.25 mag. After XB-NEWS data processing, a total of 17, 15, 14, and 15 data points in B, V, r', and i', respectively, are obtained, spanning the latter half of the IXPE campaign.

A.7. RATAN

We carried out observations of Cyg X-1 with the RATAN-600 radio telescope at 4.7 GHz and 11.2 GHz from 2023 June 16 to 24 using the "Southern Sector and Flat mirror" antenna. The sensitivity of such measurements is about 3–10 mJy beam^{-1}. Thus, Cyg X-1 was undetected most of the time, with upper limits and detections presented in Figure 1. Previous monitoring observations of Cyg X-1 have shown typical flux variations in the vicinity of 10–30 mJy at 4.7 GHz. Calibration was performed using quasar 3C 48, adopting a brightness of 5.8 and 3.42 Jy at 4.7 and 8.2 GHz, respectively, according to the flux density scale by Ott et al. (1994).

A.8. AMI

Cyg X-1 was observed 44 times in 2023 May and June with the AMI Large Array (Zwart et al. 2008; Hickish et al. 2018) at 15.5 GHz. The observations were typically ∼25 minutes, with two 10 minute scans of Cyg X-1 interleaved between short observations of a nearby compact source. The flux density scale of the observations was set by using daily short observations of 3C 286, and the interleaved calibrator observations were used

[75] https://www.isdc.unige.ch/integral/download/osa/doc/11.0/osa_um_ibis/Cookbook.html

to calibrate antenna-based amplitude and phase variations during the observations. The observations covered a 5 GHz bandwidth of a single linear polarization, Stokes $I-Q$.

A.9. Perek Telescope

Cyg X-1 was monitored in optical with the 2 m Perek Telescope located at the Ondřejov Observatory in the Czech Republic. The Ondřejov Echelle Spectrograph (OES) and the Single Order Spectrograph (CCD700) observed the source for 1 hr of exposure in the V band. Observations were first conducted just prior to the IXPE campaign on 2023 April 27 at 00:30:34 UTC, with later observations near epoch 1 on 2023 May 4 at 24:18:4 UTC, during epoch 3 on 2023 May 25 at 00:45:34 UTC, shortly before epoch 5 on 2023 June 18 at 24:22:8 UTC, and then a week after the IXPE campaign on 2023 June 29 at 21:39:44 UTC. In the Hα spectral region (6562 Å), the OES achieves a high spectral resolution of 40,000, while the CCD700 only reaches 13,000. The CCD700 is therefore principally used for calibration. For more technical information about the spectrographs, see Koubský et al. (2004) and Kabáth et al. (2020). We reduced and processed the spectra using `IRAF` software (Tody 1986, 1993). For the OES spectra, we use a semiautomatic reduction pipeline (see Cabezas et al. 2023). This pipeline includes wavelength and heliocentric calibration and continuum normalization. The disentangling method of Hadrava (2009) combines the optical spectra of the source at different orbital periods to measure the radial velocities and the orbital parameters. The Hα P Cygni profile is then isolated, and the strength factor of the line is calculated with respect to the continuum.

ORCID iDs

James F. Steiner https://orcid.org/0000-0002-5872-6061
Edward Nathan https://orcid.org/0000-0002-9633-9193
Kun Hu https://orcid.org/0000-0002-9705-7948
Henric Krawczynski https://orcid.org/0000-0002-1084-6507
Michal Dovčiak https://orcid.org/0000-0003-0079-1239
Alexandra Veledina https://orcid.org/0000-0002-5767-7253
Fabio Muleri https://orcid.org/0000-0003-3331-3794
Jiri Svoboda https://orcid.org/0000-0003-2931-0742
Kevin Alabarta https://orcid.org/0000-0003-0168-9906
Maxime Parra https://orcid.org/0009-0003-8610-853X
Yash Bhargava https://orcid.org/0000-0002-5967-8399
Giorgio Matt https://orcid.org/0000-0002-2152-0916
Juri Poutanen https://orcid.org/0000-0002-0983-0049
Pierre-Olivier Petrucci https://orcid.org/0000-0001-6061-3480
Allyn F. Tennant https://orcid.org/0000-0002-9443-6774
M. Cristina Baglio https://orcid.org/0000-0003-1285-4057
Luca Baldini https://orcid.org/0000-0002-9785-7726
Samuel Barnier https://orcid.org/0000-0002-4180-174X
Sudip Bhattacharyya https://orcid.org/0000-0002-6351-5808
Stefano Bianchi https://orcid.org/0000-0002-4622-4240
Maimouna Brigitte https://orcid.org/0009-0004-1197-5935
Mauricio Cabezas https://orcid.org/0000-0003-2050-1227
Fiamma Capitanio https://orcid.org/0000-0002-6384-3027
Jacob Casey https://orcid.org/0009-0009-3051-6570
Nicole Rodriguez Cavero https://orcid.org/0000-0001-5256-0278
Simone Castellano https://orcid.org/0000-0003-1111-4292
Elisabetta Cavazzuti https://orcid.org/0000-0001-7150-9638
Sohee Chun https://orcid.org/0009-0002-2488-5272
Eugene Churazov https://orcid.org/0000-0002-0322-884X
Enrico Costa https://orcid.org/0000-0003-4925-8523
Niccolò Di Lalla https://orcid.org/0000-0002-7574-1298
Alessandro Di Marco https://orcid.org/0000-0003-0331-3259
Elise Egron https://orcid.org/0000-0002-1532-4142
Melissa Ewing https://orcid.org/0000-0001-9349-8271
Sergio Fabiani https://orcid.org/0000-0003-1533-0283
Javier A. García https://orcid.org/0000-0003-3828-2448
David A. Green https://orcid.org/0000-0003-3189-9998
Victoria Grinberg https://orcid.org/0000-0003-2538-0188
Petr Hadrava https://orcid.org/0000-0002-4518-3918
Adam Ingram https://orcid.org/0000-0002-5311-9078
Philip Kaaret https://orcid.org/0000-0002-3638-0637
Fabian Kislat https://orcid.org/0000-0001-7477-0380
Vadim Kravtsov https://orcid.org/0000-0002-7502-3173
Brankica Kubátová https://orcid.org/0000-0002-3773-2673
Fabio La Monaca https://orcid.org/0000-0001-8916-4156
Luca Latronico https://orcid.org/0000-0002-0984-1856
Vladislav Loktev https://orcid.org/0000-0001-6894-871X
Christian Malacaria https://orcid.org/0000-0002-0380-0041
Frédéric Marin https://orcid.org/0000-0003-4952-0835
Andrea Marinucci https://orcid.org/0000-0002-2055-4946
Olga Maryeva https://orcid.org/0000-0003-1442-4755
Guglielmo Mastroserio https://orcid.org/0000-0003-4216-7936
Tsunefumi Mizuno https://orcid.org/0000-0001-7263-0296
Michela Negro https://orcid.org/0000-0002-6548-5622
Nicola Omodei https://orcid.org/0000-0002-5448-7577
Jakub Podgorný https://orcid.org/0000-0001-5418-291X
John Rankin https://orcid.org/0000-0002-9774-0560
Ajay Ratheesh https://orcid.org/0000-0003-0411-4243
Lauren Rhodes https://orcid.org/0000-0003-2705-4941
David M. Russell https://orcid.org/0000-0002-3500-631X
Miroslav Šlechta https://orcid.org/0000-0002-6819-2331
Paolo Soffitta https://orcid.org/0000-0002-7781-4104
Sean Spooner https://orcid.org/0000-0003-0710-8893
Valery Suleimanov https://orcid.org/0000-0003-3733-7267
Francesco Tombesi https://orcid.org/0000-0002-6562-8654
Sergei A. Trushkin https://orcid.org/0000-0002-7586-5856
Martin C. Weisskopf https://orcid.org/0000-0002-5270-4240
Silvia Zane https://orcid.org/0000-0001-5326-880X
Andrzej A. Zdziarski https://orcid.org/0000-0002-0333-2452
Wenda Zhang https://orcid.org/0000-0003-1702-4917
Menglei Zhou https://orcid.org/0000-0001-8250-3338
Iván Agudo https://orcid.org/0000-0002-3777-6182
Lucio A. Antonelli https://orcid.org/0000-0002-5037-9034
Matteo Bachetti https://orcid.org/0000-0002-4576-9337
Wayne H. Baumgartner https://orcid.org/0000-0002-5106-0463
Ronaldo Bellazzini https://orcid.org/0000-0002-2469-7063
Stephen D. Bongiorno https://orcid.org/0000-0002-0901-2097
Raffaella Bonino https://orcid.org/0000-0002-4264-1215
Alessandro Brez https://orcid.org/0000-0002-9460-1821
Niccolò Bucciantini https://orcid.org/0000-0002-8848-1392

Chien-Ting Chen https://orcid.org/0000-0002-4945-5079
Stefano Ciprini https://orcid.org/0000-0002-0712-2479
Alessandra De Rosa https://orcid.org/0000-0001-5668-6863
Ettore Del Monte https://orcid.org/0000-0002-3013-6334
Laura Di Gesu https://orcid.org/0000-0002-5614-5028
Immacolata Donnarumma https://orcid.org/0000-0002-4700-4549
Victor Doroshenko https://orcid.org/0000-0001-8162-1105
Steven R. Ehlert https://orcid.org/0000-0003-4420-2838
Teruaki Enoto https://orcid.org/0000-0003-1244-3100
Yuri Evangelista https://orcid.org/0000-0001-6096-6710
Riccardo Ferrazzoli https://orcid.org/0000-0003-1074-8605
Shuichi Gunji https://orcid.org/0000-0002-5881-2445
Jeremy Heyl https://orcid.org/0000-0001-9739-367X
Wataru Iwakiri https://orcid.org/0000-0002-0207-9010
Svetlana G. Jorstad https://orcid.org/0000-0001-6158-1708
Vladimir Karas https://orcid.org/0000-0002-5760-0459
Jeffery J. Kolodziejczak https://orcid.org/0000-0002-0110-6136
Ioannis Liodakis https://orcid.org/0000-0001-9200-4006
Simone Maldera https://orcid.org/0000-0002-0698-4421
Alberto Manfreda https://orcid.org/0000-0002-0998-4953
Alan P. Marscher https://orcid.org/0000-0001-7396-3332
Herman L. Marshall https://orcid.org/0000-0002-6492-1293
Francesco Massaro https://orcid.org/0000-0002-1704-9850
Chi-Yung Ng https://orcid.org/0000-0002-5847-2612
Stephen L. O'Dell https://orcid.org/0000-0002-1868-8056
Chiara Oppedisano https://orcid.org/0000-0001-6194-4601
Alessandro Papitto https://orcid.org/0000-0001-6289-7413
George G. Pavlov https://orcid.org/0000-0002-7481-5259
Abel L. Peirson https://orcid.org/0000-0001-6292-1911
Matteo Perri https://orcid.org/0000-0003-3613-4409
Melissa Pesce-Rollins https://orcid.org/0000-0003-1790-8018
Maura Pilia https://orcid.org/0000-0001-7397-8091
Andrea Possenti https://orcid.org/0000-0001-5902-3731
Simonetta Puccetti https://orcid.org/0000-0002-2734-7835
Brian D. Ramsey https://orcid.org/0000-0003-1548-1524
Oliver J. Roberts https://orcid.org/0000-0002-7150-9061
Roger W. Romani https://orcid.org/0000-0001-6711-3286
Carmelo Sgrò https://orcid.org/0000-0001-5676-6214
Patrick Slane https://orcid.org/0000-0002-6986-6756
Gloria Spandre https://orcid.org/0000-0003-0802-3453
Douglas A. Swartz https://orcid.org/0000-0002-2954-4461
Toru Tamagawa https://orcid.org/0000-0002-8801-6263
Fabrizio Tavecchio https://orcid.org/0000-0003-0256-0995
Roberto Taverna https://orcid.org/0000-0002-1768-618X
Nicholas E. Thomas https://orcid.org/0000-0003-0411-4606
Alessio Trois https://orcid.org/0000-0002-3180-6002
Sergey S. Tsygankov https://orcid.org/0000-0002-9679-0793
Roberto Turolla https://orcid.org/0000-0003-3977-8760
Jacco Vink https://orcid.org/0000-0002-4708-4219
Kinwah Wu https://orcid.org/0000-0002-7568-8765
Fei Xie https://orcid.org/0000-0002-0105-5826

References

Antia, H. M., Agrawal, P. C., Dedhia, D., et al. 2021, JApA, 42, 32
Baldini, L., Bucciantini, N., Lalla, N. D., et al. 2022, SoftX, 19, 101194
Barr, P., White, N. E., & Page, C. G. 1985, MNRAS, 216, 65P
Basak, R., & Zdziarski, A. A. 2016, MNRAS, 458, 2199
Basak, R., Zdziarski, A. A., Parker, M., & Islam, N. 2017, MNRAS, 472, 4220
Beheshtipour, B., Krawczynski, H., & Malzac, J. 2017, ApJ, 850, 14
Bhargava, Y., Bhattacharyya, S., Homan, J., & Pahari, M. 2023, ApJ, 955, 102
Bhargava, Y., Hazra, N., Rao, A. R., et al. 2022, MNRAS, 512, 6067
Bolton, C. T. 1972, Natur, 235, 271
Bramich, D. M., & Freudling, W. 2012, MNRAS, 424, 1584
Brocksopp, C., Tarasov, A. E., Lyuty, V. M., & Roche, P. 1999, A&A, 343, 861
Cabezas, M., Šlechta, M., Škoda, P., & Kubátová, B. 2023, OESRED, the Semi-automatic Reduction Code for Ondrejov Echelle Spectrograph, v1.1.1, Zenodo, doi:10.5281/zenodo.10024183
Cangemi, F., Beuchert, T., Siegert, T., et al. 2021, A&A, 650, A93
Chandrasekhar, S. 1960, Radiative Transfer (New York: Dover Publications)
Chattopadhyay, T., Kumar, A., Rao, A. R., et al. 2024, ApJL, 960, L2
Chauvin, M., Florén, H. G., Friis, M., et al. 2018, NatAs, 2, 652
Connors, P. A., Piran, T., & Stark, R. F. 1980, ApJ, 235, 224
Connors, R. M. T., García, J. A., Dauser, T., et al. 2020, ApJ, 892, 47
Cunningham, C. 1976, ApJ, 208, 534
Dauser, T., García, J., Parker, M. L., Fabian, A. C., & Wilms, J. 2014, MNRAS, 444, L100
Dauser, T., García, J., Walton, D. J., et al. 2016, A&A, 590, A76
Dauser, T., García, J. A., Joyce, A., et al. 2022, MNRAS, 514, 3965
Davis, S. W., & Hubeny, I. 2006, ApJS, 164, 530
De Marco, B., Ponti, G., Muñoz-Darias, T., & Nandra, K. 2015, ApJ, 814, 50
Dexter, J., & Begelman, M. C. 2024, MNRAS, 528, L157
Di Marco, A., Soffitta, P., Costa, E., et al. 2023, AJ, 165, 143
Dovciak, M., Steiner, J. F., Krawczynski, H., & Svoboda, J. 2023, ATEL, 16084
Dove, J. B., Wilms, J., Maisack, M., & Begelman, M. C. 1997, ApJ, 487, 759
Dovčiak, M., Muleri, F., Goosmann, R. W., Karas, V., & Matt, G. 2008, MNRAS, 391, 32
Ebisawa, K., Ogawa, M., Aoki, T., et al. 1994, PASJ, 46, 375
Fabian, A. C., Rees, M. J., Stella, L., & White, N. E. 1989, MNRAS, 238, 729
Fabian, A. C., Wilkins, D. R., Miller, J. M., et al. 2012, MNRAS, 424, 217
Fano, U. 1957, RvMP, 29, 74
Fender, R. P., Belloni, T. M., & Gallo, E. 2004, MNRAS, 355, 1105
García, J., Dauser, T., Lohfink, A., et al. 2014, ApJ, 782, 76
García, J. A., Steiner, J. F., McClintock, J. E., et al. 2015, ApJ, 813, 84
Gendreau, K. C., Arzoumanian, Z., & Okajima, T. 2012, Proc. SPIE, 8443, 844313
Gierliński, M., Zdziarski, A. A., Poutanen, J., et al. 1999, MNRAS, 309, 496
Goodwin, A. J., Russell, D. M., Galloway, D. K., et al. 2020, MNRAS, 498, 3429
Gou, L., McClintock, J. E., Reid, M. J., et al. 2011, ApJ, 742, 85
Gou, L., McClintock, J. E., Remillard, R. A., et al. 2014, ApJ, 790, 29
Grinberg, V., Pottschmidt, K., Böck, M., et al. 2014, A&A, 565, A1
Haardt, F. 1993, ApJ, 413, 680
Hadrava, P. 1997, A&AS, 122, 581
Hadrava, P. 2009, arXiv:0909.0172
Harrison, F. A., Craig, W. W., Christensen, F. E., et al. 2013, ApJ, 770, 103
Hickish, J., Razavi-Ghods, N., Perrott, Y. C., et al. 2018, MNRAS, 475, 5677
Ichimaru, S. 1977, ApJ, 214, 840
Jana, A., & Chang, H.-K. 2024, MNRAS, 527, 10837
Jourdain, E., Roques, J. P., Chauvin, M., & Clark, D. J. 2012, ApJ, 761, 27
Kaastra, J. S., & Bleeker, J. A. M. 2016, A&A, 587, A151
Kabáth, P., Skarka, M., Sabotta, S., et al. 2020, PASP, 132, 035002
Koubský, P., Mayer, P., Čáp, J., et al. 2004, PAICz, 92, 37
Kravtsov, V., Veledina, A., Berdyugin, A. V., et al. 2023, A&A, 678, A58
Krawczynski, H. 2012, ApJ, 754, 133
Krawczynski, H., & Beheshtipour, B. 2022, ApJ, 934, 4
Krawczynski, H., Muleri, F., Dovčiak, M., et al. 2022, Sci, 378, 650
Laor, A. 1991, ApJ, 376, 90
Laurent, P., Rodriguez, J., Wilms, J., et al. 2011, Sci, 332, 438
Lebrun, F., Leray, J. P., Lavocat, P., et al. 2003, A&A, 411, L141
Li, L.-X., Zimmerman, E. R., Narayan, R., & McClintock, J. E. 2005, ApJS, 157, 335
Loktev, V., Veledina, A., Poutanen, J., Nättilä, J., & Suleimanov, V. F. 2024, A&A, 685, A84
Loktev, V., Veledina, A., & Poutanen, J. 2022, A&A, 660, A25
Long, K. S., Chanan, G. A., & Novick, R. 1980, ApJ, 238, 710
Madsen, K. K., Beardmore, A. P., Forster, K., et al. 2017, AJ, 153, 2
Madsen, K. K., Grefenstette, B. W., Pike, S., et al. 2020, arXiv:2005.00569
Marra, L., Brigitte, M., Rodriguez Cavero, N., et al. 2024, A&A, 684, A95
McClintock, J. E., Shafee, R., Narayan, R., et al. 2006, ApJ, 652, 518

McConnell, M. L., Zdziarski, A. A., Bennett, K., et al. 2002, ApJ, 572, 984
Méndez, M., Karpouzas, K., García, F., et al. 2022, NatAs, 6, 577
Miller-Jones, J. C. A., Bahramian, A., Orosz, J. A., et al. 2021, Sci, 371, 1046
Mirabel, I. F., & Rodrigues, I. 2003, Sci, 300, 1119
Misra, R., Roy, J., & Yadav, J. S. 2021, JApA, 42, 55
Oda, M. 1977, SSRv, 20, 757
Orosz, J. A., McClintock, J. E., Aufdenberg, J. P., et al. 2011, ApJ, 742, 84
Ott, M., Witzel, A., Quirrenbach, A., et al. 1994, A&A, 284, 331
Podgorný, J., Marra, L., Muleri, F., et al. 2023, MNRAS, 526, 5964
Poutanen, J., & Coppi, P. S. 1998, PhyS, T77, 57
Poutanen, J., & Svensson, R. 1996, ApJ, 470, 249
Poutanen, J., Veledina, A., & Beloborodov, A. M. 2023, ApJL, 949, L10
Ratheesh, A., Dovčiak, M., Krawczynski, H., et al. 2024, ApJ, 964, 77
Reeves, J., Done, C., Pounds, K., et al. 2008, MNRAS, 385, L108
Remillard, R. A., Loewenstein, M., Steiner, J. F., et al. 2022, AJ, 163, 130
Remillard, R. A., & McClintock, J. E. 2006, ARA&A, 44, 49
Rodriguez Cavero, N., Marra, L., Krawczynski, H., et al. 2023, ApJL, 958, L8
Rodriguez, J., Grinberg, V., Laurent, P., et al. 2015, ApJ, 807, 17
Russell, D. M., Bramich, D. M., Lewis, F., et al. 2019, AN, 340, 278
Schnittman, J. D., & Krolik, J. H. 2009, ApJ, 701, 1175
Schnittman, J. D., & Krolik, J. H. 2010, ApJ, 712, 908
Singh, K. P., Stewart, G. C., Chandra, S., et al. 2016, Proc. SPIE, 9905, 99051E
Singh, K. P., Stewart, G. C., Westergaard, N. J., et al. 2017, JApA, 38, 29
Singh, K. P., Tandon, S. N., Agrawal, P. C., et al. 2014, Proc. SPIE, 9144, 91441S
Steiner, J. F., García, J. A., Eikmann, W., et al. 2017, ApJ, 836, 119
Steiner, J. F., Narayan, R., McClintock, J. E., & Ebisawa, K. 2009, PASP, 121, 1279
Steiner, J. F., Reis, R. C., McClintock, J. E., et al. 2011, MNRAS, 416, 941
Stetson, P. B. 1990, PASP, 102, 932
Stirling, A. M., Spencer, R. E., de la Force, C. J., et al. 2001, MNRAS, 327, 1273
Sunyaev, R. A., & Titarchuk, L. G. 1985, A&A, 143, 374
Svoboda, J., Dovčiak, M., Steiner, J. F., et al. 2024a, ApJ, 960, 3
Svoboda, J., Dovčiak, M., Steiner, J. F., et al. 2024b, ApJL, 966, L35
Tananbaum, H., Gursky, H., Kellogg, E., Giacconi, R., & Jones, C. 1972, ApJL, 177, L5
Taverna, R., Zhang, W., Dovčiak, M., et al. 2020, MNRAS, 493, 4960
Tody, D. 1986, Proc. SPIE, 627, 733
Tody, D. 1993, in ASP Conf. Ser. 52, Astronomical Data Analysis Software and Systems II, ed. R. J. Hanisch, R. J. V. Brissenden, & J. Barnes (San Francisco, CA: ASP), 173
Tomsick, J. A., Nowak, M. A., Parker, M., et al. 2014, ApJ, 780, 78
Tomsick, J. A., Parker, M. L., García, J. A., et al. 2018, ApJ, 855, 3
Tonry, J. L., Denneau, L., Heinze, A. N., et al. 2018, PASP, 130, 064505
Veledina, A., & Poutanen, J. 2022, Polarization of Comptonized Emission in Slab Geometry, v1, Zenodo, doi:10.5281/zenodo.7116125
Walton, D. J., Tomsick, J. A., Madsen, K. K., et al. 2016, ApJ, 826, 87
Wang, J., Kara, E., Lucchini, M., et al. 2022, ApJ, 930, 18
Webster, B. L., & Murdin, P. 1972, Natur, 235, 37
Weisskopf, M. C., Silver, E. H., Kestenbaum, H. L., et al. 1977, ApJL, 215, L65
Weisskopf, M. C., Soffitta, P., Baldini, L., et al. 2022, JATIS, 8, 026002
Wilms, J., Allen, A., & McCray, R. 2000, ApJ, 542, 914
Yadav, J. S., Agrawal, P. C., Antia, H. M., et al. 2016, Proc. SPIE, 9905, 99051D
Yadav, J. S., Agrawal, P. C., Antia, H. M., et al. 2017, CSci, 113, 591
Zdziarski, A. A., Chand, S., Banerjee, S., et al. 2024, ApJL, 967, L9
Zdziarski, A. A., Johnson, W. N., & Magdziarz, P. 1996, MNRAS, 283, 193
Zdziarski, A. A., Shapopi, J. N. S., & Pooley, G. G. 2020, ApJL, 894, L18
Zhang, S. N., Cui, W., & Chen, W. 1997, ApJL, 482, L155
Zhao, X., Gou, L., Dong, Y., et al. 2021, ApJ, 908, 117
Zwart, J. T. L., Barker, R. W., Biddulph, P., et al. 2008, MNRAS, 391, 1545
Życki, P. T., Done, C., & Smith, D. A. 1999, MNRAS, 309, 561